

硕士学位论文

(学术学位论文)

基于空间多点探测的物理场的一次和二次梯度算法的分析研究

**STUDY ON ALGORITHMS FOR THE LINEAR AND
QUADRATIC GRADIENTS OF PHYSICAL FIELDS
BASED ON MULTIPOINT MEASUREMENT IN
SPACE**

周宇飞

哈尔滨工业大学

2021 年 12 月

国内图书分类号: O53
国际图书分类号: 52

学校代码: 10213
密级: 公开

理学硕士学位论文

基于空间多点探测的物理场的一次和二次梯度算法的设计研究

硕 士 研 究 生: 周宇飞

导 师: 沈超 教授

申 请 学 位: 理学硕士

学 科: 物理学

所 在 单 位: 哈尔滨工业大学(深圳)

答 辩 日 期: 2021 年 12 月

授予学位单位: 哈尔滨工业大学

Classified Index: O53
U.D.C: 52

A dissertation submitted in partial fulfillment of
the requirements for the academic degree of
Master of Science

**STUDY ON ALGORITHMS FOR THE LINEAR AND
QUADRATIC GRADIENTS OF PHYSICAL FIELDS
BASED ON MULTIPOINT MEASUREMENT IN
SPACE**

Candidate:	Yufei Zhou
Supervisor:	Prof. Chao Shen
Academic Degree Applied for:	Master of Science
Specialty:	Physics
Affiliation:	Harbin Institute of Technology, Shenzhen
Date of Defense:	December, 2021
Degree-Conferring-Institution:	Harbin Institute of Technology

摘要

随着 Cluster、MMS 等多卫星联合探测计划的实现，多点探测，作为空间科学探测研究的新技术、新方法，已经为推动空间科学发展起到重大作用。为了配合多点探测计划对空间中物理场的几何结构进行研究，学者们已经建立了一系列基于多卫星探测的数学算法，其中应用较为广泛的有卷曲计、磁曲率分析、磁旋转分析。这些分析方法都是基于物理场的一次梯度计算，将之和其他物理场量按照一定方式组合，对一些不能在空间中用单卫星或双卫星直接测量的物理量进行估计。然而当前空间中仍然有许多物理量不能通过现有的多卫星探测算法获得，这是因为它们依赖于物理场的二次梯度，比如磁重联过程中磁场扩散依赖于磁场的二次梯度。另外，在深空探测领域，多卫星联合探测还未实现。国际普遍的做法是发射单颗探测卫星离开地球进行探测。而现有的多卫星探测算法不能直接应用于单卫星探测物理场的一次和二次梯度。所以我们希望能够建立新的多点算法对物理场的二次梯度进行估计。这种算法应该既在多卫星计划中可行，又能在单卫星计划中发挥作用。

通过研究不同的差分方法，我们发现简单地将单变量差分应用于空间物理场的二次梯度算法建立虽然可行，但是是建立在损失大量精度的前提下。现有研究表明，想要建立普适而又高精度的算法，需要利用泰勒定理获取物理场的一次和二次梯度并使用最小二乘法将算法的截断误差降到最低。

本文论述了 ALQG 方法，一个基于多点探测估计物理场的一次梯度和二次梯度的不含时间算法，并且基于此建立了一个含时间算法。这里的场可以是标量场、矢量场，也可以是更高阶的张量场。这里的一个探测点既可以是一颗探测卫星，也可以某颗卫星上的一个探测仪器。第一个算法是不含时的，即该算法需要的输入数据必须是同时测量的。这个算法需要十个及以上数量的在不同空间位置测量的场的数据作为输入，能估计探测点群，即测量点位置群，几何中心附近位置的场的一次梯度和二次梯度。其中对几何中心处的估计最为准确。第二个算法是含时的，即该算法的输入数据可以是异时测量的。利用至少十五个在不同空间位置不同时间时刻上测量的物理场数据作为输入，该算法能够估计位于探测数据群时空中心附近时间-空间位置处的物理场的一次梯度和二次梯度。其中对探测数据群时空中心处的估计最为准确。此算法估计得的一次和二次梯度也是在四维时空中的梯度。

不含时算法的推导基于泰勒公式和最小二乘法，给出一组在三维空间中的张量估计方程。求解这组张量估计方程就能获得对目标点处物理场的一次梯度和二次梯度的估计。这组方程的求解有两种方法。一种方法需要将该张量估计方程组转化为一个系数矩阵阶数为 10×10 的线性方程组，求解这个线性方程组即可实现对一次和二次梯度的估计。这种求解方法可以拓展到更高阶物理场梯度的计算。另一种方法根据微扰理论的思想对该张量方程组进行迭代计算，在过程中将一个四阶张量方程降阶为一个二阶张量方程，并求解这个二阶张量方程。该方程是探测点群的一个特征线性系统，其特征系数矩阵由探测点群的分布完全决定，且对算法的截断误差有着决定性影响。当它的本征值只有一个非零时，探测点群对应于线性分布，算法只能求得一个方向上的一次梯度和二次梯度。当它的本征值只有三个非零时，探测点群对应于平面分布，算法只能求得两个方向上的一次梯度和二次梯度。所以这个特征矩阵能用于判断探测点群分布的优劣，从而对误差有一定预估。

含时算法的推导过程类似于不含时算法，也是基于泰勒公式和最小二乘法，给出一组在四维时空中的张量方程，用于对物理场的一次梯度和二次梯度进行估计。针对这一组张量方程，同样有两种求解方法。一种方法将该张量方程组转化为一个系数矩阵阶数为 15×15 的线性方程组，求解这个线性方程组即可实现估计。另一种方法对该张量方程组进行迭代计算，在过程中辅以求解一个特征线性系统。这里的特征线性系统由探测数据的时空分布完全决定，且对算法的截断误差有着决定性影响。当它的本征值只有一个非零时，探测点群对应于四维时空中的线性分布，算法只能求得一个方向上的一次梯度和二次梯度。这个方向可能是纯时间的，可能是纯空间的，也可能是时间空间混合的。当特征矩阵的本征值只有三个非零时，探测点群对应于平面分布，算法只能求得两个方向上的一次梯度和二次梯度，这两个方向可能是纯空间的，也可能是时间空间混合的。当特征矩阵的本征值只有六个非零时，探测点群对应于三维超平面分布，算法只能求得三个方向上的一次梯度和二次梯度。这三个方向可能是纯空间的，也可能是时间空间混合的。这个特征矩阵能用于判断探测数据时空分布的优劣。

我们在磁通量绳磁场、偶极子磁场和磁层磁场模型这三个磁场模型中对不含时算法的迭代求解方法进行了模拟。部分模拟采用相同探测点群，研究迭代次数与收敛的关系，研究算法误差与相对单侧尺度的关系。部分模拟采用相同相对探测尺度，研究算法误差与探测点数的关系。模拟结果证实了该算法这种求解方

法的可行性、高效性、可靠性和高精度。

基于一个十五点的探测点群，我们将得到的十五个模拟同时测得的探测数据输入不含时算法并求得探测点群几何中心处的磁场的一次梯度和二次梯度。在迭代过程中，我们发现经过第一次迭代，算法给出的一次梯度和二次梯度估计中包含的误差已经大幅下降，经过少于五十次的迭代计算，所有模型中算法给出的估计都明显达到收敛。而这些模型中磁场的五十次迭代计算耗时小于 0.05 秒。由此可见迭代算法是可行的，而且是高效快速的。

采用同样的十五点探测点群，在三个磁场模型的模拟中，通过放大缩小探测点群的尺度从而调节一次模拟的相对探测尺度，我们发现物理场的二次梯度估计的相对误差随相对探测尺度以一次幂形式增长，即线性增长，物理场的一次梯度估计的相对误差随相对探测尺度以二次幂形式增长。在磁通量绳磁场模型中，对所模拟的相对探测尺度范围，即从 $L/D = 0.01$ 到 $L/D = 0.6$ ，磁场一次梯度和二次梯度估计以及由它们计算所得的磁力线曲率和挠率估计的相对误差基本上都小于百分之五。在偶极子磁场模型的模拟中，当相对探测尺度小于 0.1 时，磁场的一次梯度估计相对误差和磁力线曲率估计相对误差都小于百分之五。当相对探测尺度小于 0.01 时，磁场的二次梯度各分量估计的相对误差都小于百分之五。在磁层磁场模型的模拟中，当相对探测尺度小于 0.1 时，磁场的一次梯度估计相对误差和磁力线曲率估计相对误差都小于 5%。当相对探测尺度小于 0.01 时，磁场的二次梯度即磁力线挠率估计的相对误差都小于百分之五。不含时算法的迭代求解方法在这三个由简单到复杂的矢量场模型中，在不同的相对探测尺度下，都显示出良好的精度。这证明了该算法的可靠性和高精度。

控制相对探测尺度和探测位置这两个变量，通过生成不同探测点数量的探测点群，我们研究了不含时算法迭代求解方法与探测点数量的关系。在磁层磁场模型的模拟中我们发现，磁场二次梯度各分量估计中包含的平均相对误差与探测点的数量呈反比关系，而其一次梯度个分量估计中包含的平均相对误差与探测点的数量无明显关系。

多点探测方法在空间中可以应用在单卫星多探测仪器的采集数据上，也可以应用在多卫星的联合探测上。若多卫星联合探测的卫星数目较多，很难在不同卫星间实现探测时间同步，即此时探测得的数据是不同时的，不含时算法应用受到一定限制。我们提出含时算法希望能够处理这种情况，既对空间的一次梯度和二次梯度进行估计，也对包含时间的梯度分量进行估计。由于该含时算法还未得

到模拟验证，还不宜在实际中应用。我们的工作能对现有现有的空间多点探测计划数据分析研究起到一定推进作用。

关键词：多点探测；一次梯度；二次梯度；算法

ABSTRACT

Multipoint measurement techniques based on four or more points have achieved great success in deducing physical quantities related to linear gradients of other physical fields and unattainable through single-point measurement in space. Yet several other quantities, such as charge density, diffusion of magnetic fields, and torsion of magnetic field lines, which are related to quadratic gradients of physical fields, are not acquirable, if various physical constraints are not introduced to reduce the freedom in the specific problems.

In this study, a general algorithm that can estimate spatial linear as well as quadratic gradients of physical fields building on multiple measurements of the fields themselves is comprehensively reviewed, and building on it a general algorithm that can estimate temporo-spatial linear and quadratic gradients is developed. One, the time-independent algorithm, utilizing at least ten simultaneous measurements, can estimate the linear and quadratic gradients in the vicinity of the constellation's geometric center. The other, the time-dependent algorithm, taking at least fifteen non-temporally-synchronized measurements as input, can estimate them near the spatial-temporal center in four-dimensional space-time domain. Two schemes for solving the estimating equations of each algorithm are put forward. Using simulations of the time-independent algorithm on force free flux rope magnetic field, dipole magnetic field, and a modeled magnetospheric magnetic field, we confirm the great efficiency, strong robustness, and high accuracy of the algorithm. The estimation based on fifteen measurements generally costs less than 0.05s. The algorithm successfully gives estimations of low error for all the three physical fields. The accuracy for estimating the linear gradient is of second order, and for the quadratic gradient is of first order. The truncation error of the algorithm for quadratic gradient is inversely proportional to the number of measurements, with which that for linear gradient, though, shows no conspicuous relationship. The time-dependent algorithm as yet remain untested, and therefore is not suggested to be applied. The time-independent algorithm could be widely applied to both space exploration mission and instrument designs in the future, and to the analysis of the data acquired by multipoint measurements currently.

Keywords: multipoint measurement, linear gradient, quadratic gradient, algorithm

ACKNOWLEDGEMENT

I would like to pay my due greatest compliments to my supervisor, Prof. Shen Chao, on the great care, which he took of my study and research, and on his unwearied perseverance and constancy in all his friendships. I still remember the equations he wrote on paper when I discussed with him on research for the first time. It was on his papers and through countless hours of helpful discussions that he taught me independent thinking and guided me along my journey of colorful graduate student life. Not only did his profound knowledge and innovative ideas benefit me a lot, but his patience and encouragement also helped me go through frustrations. He has been very supportive when I came across difficulties and I would not have been able to make it without his priceless trust. It is my great privilege to have his mentorship during this journey.

I would like to extend my sincere thanks to Prof. Pingbing Zuo for introducing me to the space physics not only as the subject of a course but also as a research field and community. I would also like to thank Prof. Chaowei Jiang for his rigorous teaching on magnetohydrodynamical principles and various magnetic structures and dynamical activities in the solar atmosphere. I am also grateful to Prof. Gang Qin for the plasma physical principles and mathematical formulations I learned from him, which lays down the basis of this research. I really appreciate Prof. Yi Wang and Prof. Mingyu Wu for their innovative and informative courses on various physical structures and processes in the heliosphere and the magnetosphere and Prof. Zhibin Yu for all knowledge about the measurement techniques in space that he imparted to me.

I would like to express my sincere gratitude to my friends, Jinye Zhu, Nian Ren, Lai Gao, Peng Shao, Yuhang Mu, Yalan Chen and etc for all the supports, laughter, and joy.

To my parents. Words cannot express my gratitude.

CONTENTS

	Page
Abstract	V
Acknowledgement	VII
Contents	VIII
List of Tables	X
List of Figures	XI
Nomenclature	XII
1 Introduction	1
1.1 Measurements in space physics	1
1.2 Applications of multiple points measurement	3
1.3 Motivation and objectives	6
1.3.1 On charge density	7
1.3.2 On magnetic reconnection	8
1.3.3 On the torsion of magnetic field lines	9
1.4 The research contents of the dissertation	10
2 General Algorithms for the Linear and Quadratic Gradients of Physical Fields	11
2.1 Introduction	11
2.2 Basics of numerical differentiation	12
2.3 A rudimental consideration for simultaneous measurements	14
2.4 The time-independent algorithm	15
2.4.1 Approximating in three-dimensional space	16
2.4.2 The estimating equations	17
2.4.3 Solving the estimating equations by linear system solvers	19
2.4.4 Solving the estimating equations by an iterative method	21
2.4.5 Reducing tensor order	22
2.4.6 The characteristic matrices of the distribution of measurement points	24
2.5 Proof of the Required Number of Points at a Minimum	28
2.6 The time-dependent algorithm	31
2.7 Summary and discussion	35

3 Testing the Time-independent Algorithm	38
3.1 Introduction	38
3.2 The configuration of the constellation	39
3.3 Magnetic flux rope	41
3.4 Dipole magnetic field	46
3.5 Modeled magnetospheric field	49
3.6 Summary and discussion	54
Conclusions	55
References.....	57
Innovative achievements for Master	67
哈尔滨工业大学学位论文原创性声明和使用权限	68

LIST OF TABLES

Table	Page
3–1 The distribution of the fifteen measurement points for time-independent algorithm's modeling.....	40
3–2 The eigenvalues of the characteristic matrix \mathcal{R}	41

LIST OF FIGURES

Figure	Page
3.1 The distribution of the fifteen measurement points for time-independent algorithm's modeling.	40
3.2 Relative errors of the non-vanishing components of the LQGs in the force-free flux rope magnetic field computed by different numbers of iterations.	43
3.3 Relative errors in estimating the LQGs and curvature and torsion of the magnetic field lines of flux rope magnetic field by relative measurement scale.	45
3.4 Relative errors of the non-vanishing components of the linear and quadratic gradients of magnetic dipole field computed by different numbers of iterations. .	47
3.5 Relative errors in estimating the LQGs and curvature of the magnetic field lines of dipole magnetic field by relative measurement scale.	48
3.6 Magnetic field lines of the MMF in the $x - z$ plane.	50
3.7 Relative errors of the non-vanishing components of the linear and quadratic gradients of the MMF computed by different numbers of iterations.	51
3.8 Relative errors in estimating the LQGs and curvature and torsion of the magnetic field lines of MMF by relative measurement scale.	52
3.9 Averaged relative errors of estimating LQGs of the MMF by different number of measurements.	53

NOMENCLATURE

Dst	Disturbance Storm Time
LQGs	Linear and Quadratic Gradients
MMF	Modeled Magnetospheric Field
MCA	Magnetic Curvature Analysis
MRA	Magnetic Rotation Analysis
NFA	Normal Field Analysis
THEMIS	Time History of Events and Macroscale Interactions during Substorms
MMS	Magnetospheric Mutiscale

CHAPTER 1

INTRODUCTION

1.1 Measurements in space physics

Many significant discoveries in human history come in the wake of unprecedented measurements.

The first measurement made in the field of space physics is traced to the Chinese who discovered the compass's fundamentals. Following the invention of the device which measures the direction of the ambient magnetic field on the ground, in the 16th century the explanation by William Gilbert^[1] on compass needles pointing at north resulted in the notion of the Earth's magnetic field. Magnetic storm which reveals itself in the increasing and decreasing of geomagnetic fields are first learned through detailed research conducted by George Graham^[2] in the 18th century on the variation of the angle between the north, the direction along a meridian towards the geographic North pole, and the magnetic north at which compass needle pointed. The first absolute magnetometer that can also determine the strength of the magnetic field is devised by C. F. Gauss in 1832. And the ability to obtain the magnetic flux intensity further prompted the research concerning the magnetic storm later on. A simple example is the disturbance storm time (Dst) index^[3] derived from the magnetic measurements at four ground stations near the equator. It is the averaged station measurements weighted by the average cosines of the magnetic latitude of the stations, as defined by

$$Dst(T) = \frac{\sum_n^4 D_n(T)}{\sum_n^4 \cos \phi_n},$$

where $D_n(T)$ is the disturbance of the magnetic field at the n th station. The Dst index reflects the variation of the total energy of the ring current particles around Earth caused by geomagnetic activities and therefore becomes a good indicator for the geomagnetic storm^[4, 5].

Another device that has an old history as the compass is the telescope invented at the beginning of the 17th century and utilized to observe celestial bodies, in particular the Sun. The superficial feature on the Sun known as sunspots was discovered by ancient Chinese with their naked eye. However, not until the invention of the telescope were sys-

tematic studies conducted by astronomers like Galileo Galilei and Christoph Scheiner^[6]. With the improvement of the quality of observation, S. H. Schwabe in 1843 made a huge discovery^[6], the sunspot cycle of 11 years which lead to the notion of the solar cycle^[7, 8]. Solar cycle plays a key role in human's understanding relating solar activities^[9], such as solar flares^[10], prominence eruptions^[11], and coronal mass ejections^[12], to their terrestrial effects on planets like magnetic storms^[13, 14], substorms^[15], and aurorae^[16], because it is the very cycle that determines all the cycle of these solar and planetary phenomena. It also determines the cycle of the heliospheric magnetic field's geometry^[17], the shape of the heliospheric current sheet^[18], and the mean speed of solar wind and its distribution in the heliosphere^[19]. Besides, The intensity of energetic particles of solar origin and galactic origin (called galactic cosmic rays) both varies at the time scale of the solar cycle^[20]. The prediction of the forthcoming solar cycles, or solar activity cycles, has therefore long been of interest^[21–23].

The late 1950s saw the advent of an entirely new era of space physics on account of human's success in taking measurements in space. In 1958, by taking advantage of powerful propulsion provided by new rocket technology, the United States sent its first space exploration spacecraft, Explorer 1, into space, on which a cosmic ray detector is boarded. The very existence of radiation belts was thereafter theorized by J. A. Van Allen to explain an unexpected high counting rate seen by the Geiger counters on Explorer 1^[24, 25]. This is widely thought of as the event signaling the dawn of the new era. Not only have particle detectors onboard spacecraft made groundbreaking discoveries about the nature of the space, but electric and magnetic fields probes also have had major contributions to the understanding of it. For example, the already predicted existence of the magnetopause^[26] about ten Earth's radii (R_E) ahead toward the Sun and tens of R_E surrounding the Earth was first confirmed by the observation with a three-component magnetometer carried on Explorer 12^[27] which was launched in 1961 as one of the earliest artificial spacecraft.

Further improvements in space technologies, especially on rocket propulsions, made possible the missions that reached deeper into space. Pioneer 5, launched in 1960, was the first, among its peers in spacecraft boomers years to measure electric and magnetic field phenomena, solar flare particles, and ionization in the interplanetary region. Mariner 2, as an interplanetary probe launched in 1962, was the first to visit another planet, Venus,

in the solar system. Voyager 1, as intended to investigate the outer solar system and interstellar space beyond the heliosphere, was launched in 1977, crossed the heliopause in 2012, and remains active so far. The Parker Solar Probe launched in 2018, protected by a solar shield from the ultra-hot solar atmosphere, provides an opportunity to observe the Sun at the closest distance ever possible. These space probe missions define quite well the spatial regime of in situ measurement.

Measurement techniques in space plasmas, according to the object of the measurement, are classified into two main categories, for fields measurement and plasma particles measurement. Fields measurement^[28] can further divide into the measurements of electric fields, magnetic fields, and space plasma waves. Space plasma wave measurement is a special and big technique in that, taking advantage of the propagational ability of waves, remote sensing that can draw complete pictures of the plasmas in the "sphere" concerned, such as the magnetosphere of the Earth and the photosphere of the Sun, can be implemented. In the remit of particle measurement^[29], a slew of novel techniques are applied to measure various properties of particles of most kinds. Langmuir probes are used to determine the electron density and temperature. Retarding potential analyzers are used to analyze the energy distribution of ions. Particle spectrometers, as a large combination of various designs, measure the distribution function of ions as well as electrons. Particle correlator measures the oscillations in particle distribution produced by wave-particle interaction. Energetic particles spectrometers are devoted to measuring elusive energetic particles, including electrons and ions of high energy.

1.2 Applications of multiple points measurement

At the dawn of the new millennium, the Cluster mission ushered in a new page of the history of measurements in space, that is, the application of four-point measurement, the most advanced version of multipoint measurement.

Multipoint measurement had been well-known for decades. The first version of multipoint measurement in space is two-point measurement. Although no mission made up of four spacecraft in a close constellation had been available until Cluster, there were occasions where some spacecraft's orbits intersected in the same region at the same time, and few missions, like ISEE, which offered two spacecraft flying in tandem. All these

occasions and missions provided good chances to investigate various physical properties not attainable through single spacecraft measurement that cannot distinguish between spatial and temporal phenomena. In 1988, Z. Němeček et al.^[30] studied the velocities of the Earth's bow shock using simultaneous measurements by two intermittently closely separated spacecraft, Prognosz 10 and IMP-8. In a similar manner by using two-point measurements, numerous works were done in analyzing the speed and thickness of, in addition to the bow shock^[31], a variety of discontinuities and/or surfaces in space, such as the Earth's magnetopause^[32], dipolarization fronts^[33], and the current sheet^[34, 35] in the Earth's magnetotail. Moreover, the gradients of physical quantities in space were also investigated using two-point measurements. For example, the plasma density gradient near the magnetopause was investigated using simultaneous Interball 1 and Magion observation^[36].

Yet studies using information simultaneously obtained by two spacecraft are restricted to one-dimensional views, even though they differentiate between time and space. The bow shock's velocity as well as its normal under the assumption of its contraction and expansion motion, for instance, are vectors comprising three components. Only one component can be obtained from two-spacecraft measurement, while the other components perpendicular to the beeline connecting the measurement points are not attainable.

To address this problem, Cluster, consisting of four spacecraft, was designed to ascertain the complete spatial and temporal variations in physical quantities and three-dimensional velocities of the discontinuities and/or surface in space^[37–39]. Using more than 500 bow shock crossings by Cluster from 2001 to 2013 and a full timing method, O. Krukarova et al. investigated the distribution of the bow shock velocities under a wide range of solar wind conditions^[40]. Using Cluster crossing of the magnetopause, S. E. Haaland et al. investigated the orientation, motion, and thickness of the magnetopause^[41]. The motion of dipolarization front and the flapping of current sheet were also intensively studied using Cluster data^[42, 43].

Since all components of the gradient of a physical quantity, be it a scalar or vectorial field, are achievable through four-point measurement^[44], a trove of novel techniques for data analysis based on them in space physics are developed^[45–52]. And these methods have found wide application in space exploration. Here we briefly introduce three important techniques.

The curlometer technique^[45] builds on the Ampère's law,

$$J_{ck} = \frac{1}{\mu_0} \epsilon_{ijk} B_{i,j}, \quad (1.1)$$

where ϵ_{ijk} is the Levi-Civita symbol in three dimensions. Note that a comma in the subscript indicates a partial differentiation, $B_{i,j} = \partial_j B_i$, and that the Einstein summation convention is used here and in the rest of this dissertation. According to this convention, when an index variable appears twice in a single term and is not otherwise defined (see free and bound variables), it implies a summation of that term over all the values of the index. The technique is extensively and successfully utilized to study the current system in the Earth's magnetosphere, including the ring current^[53], the magnetic field-aligned current^[54], the Chapman-Ferraro current^[55], and the current sheet in magnetotail^[56], from large to small scales^[57].

Magnetic curvature analysis (MCA)^[46] and magnetic rotation analysis (MRA)^[48] are two sophisticated and well-developed algorithms for analyzing the three-dimensional topology of magnetic fields. The MCA, utilizing the definition of a curve's curvature,

$$\rho_{cj} = b_i b_{j,i}, \quad (1.2)$$

where $\mathbf{b} = \mathbf{B}/B$ is the normalized vector of magnetic fields and hence the unit tangent vector of magnetic field lines, is devoted to deducing the curvature radius, the normal, and the binormal of magnetic field lines. The MRA, promoting and based on the magnetic rotation tensor,

$$S_{ij} = b_{l,i} b_{l,j}, \quad (1.3)$$

is a tool for the examination of magnetic fields' rotational features. They are applied to the investigation of the multifarious magnetic structures widespread in the magnetosphere, such as magnetic reconnection sites^[58], the current sheet^[59], flux tubes^[60], Kelvin-Helmholtz waves^[61, 62], the Earth's bow shock^[51], and magnetic holes in the solar wind^[63].

Normal field analysis (NFA)^[51] is a new tool for the analysis of boundaries in space. It extends the geometrical and topological analysis of curves using MCA and MRA to surfaces. A moving boundary produces a family of surfaces, with which the space near crossing sites by spacecraft on orbit is filled up, and to which a field of normal is attached. By supposing that all the surfaces are close to a plane, it is found that the principal curvatures

of these surfaces at each point are equal to the eigenvalues of the gradient matrix of the normal field. In mathematical formulation, a surface in three-dimensional space is usually defined by $S(u, v) = [x(u, v), y(u, v), z(u, v)]$, and the normal field on the surface is defined by $\mathbf{n}(u, v) = [n_x(u, v), n_y(u, v), n_z(u, v)]$. The family of surfaces and the family of normals can be written as $S(u, v, t) = [x(u, v, t), y(u, v, t), z(u, v, t)]$ and $\mathbf{n}(u, v, t) = [n_x(u, v, t), n_y(u, v, t), n_z(u, v, t)]$ where t is the temporal variable whose range is limited by some start point and end point of the boundary's motion. The parametrization of the family of surfaces, theoretically, can be totally determined by a new parametrization $[u(x, y, z), v(x, y, z), t(x, y, z)]$. The family of normal fields on the surfaces, which in effect is another normal field in three-dimensional Euclidean space, in terms of the new parametrization, becomes $\mathbf{n}(x, y, z) = [n_x(x, y, z), n_y(x, y, z), n_z(x, y, z)]$. The gradient of this field, $\nabla \mathbf{n}$ or $n_{i,j}$, where the Latin characters i and j ranging from 1 to 3 indicate the three dimensions x, y, z , is in three-dimensional space. The gradient of the normal field has three eigenvalues, λ_i , $1 \leq i \leq 3$ with $|\lambda_i| \geq |\lambda_j|$ for all $i > j$. In theory, the eigenvalue $\lambda_1 = 0$ and the other two are non-zeros. If the local surface is akin to a planar one, the eigenvector corresponding to the zero eigenvalue λ_1 is the normal itself, $\mathbf{e}_1 = \mathbf{n}$. The other two eigenvectors and corresponding eigenvalues are the principal directions and the principal curvatures of the surface. Since the gradient of the curvature field is calculable, it is easy to achieve the principal curvatures and directions that are basic topological parameters of a surface, or a boundary in space physical terminology. This newly developed technique has been used to investigate, as its first application, the surficial properties of dipolarization fronts in the Earth's magnetotail^[51].

Following Cluster, Time History of Events and Macroscale Interactions during Substorms (THEMIS)^[64] launched in 2007 and Magnetospheric Multiscale (MMS)^[65] launched in 2015, along with computer simulation^[66], offers abundant opportunities to utilize these techniques and discover new physics.

1.3 Motivation and objectives

The techniques for estimating the linear gradient of physical fields and calculating various quantities based on them have led to a lot of monumental achievements in space physics. However, some other physical quantities, such as charge density, the Laplacian

of magnetic field, and the torsion of the magnetic field lines, are hard to calculate in a complete sense either due to large measurement errors with current techniques or because some assumptions have to be made to obtain them^[67, 68]. Through an analysis below in this section, we shall realize that it is the quadratic gradients of physical fields that form the basis of calculating these quantities. And general algorithms of high accuracy for estimating the quadratic gradient based on multipoint measurement should be developed to foster further groundbreaking discoveries and progresses in observational and experimental space physics.

1.3.1 On charge density

Particles are omnipresent in the universe. As for the near space around the Earth, protons, alpha particles and electrons are of most interest. A series of particle detectors are designed and developed by many talented physicists and engineers^[29]. The data acquired by these detectors are usually in the form of the distribution function of the aimed particles, which generally contain all information about the velocity, density, momentum, kinetic energy of the particles as a fluid.

However, previous investigation conducted by Kaufmann et al^[69, 70] suggest that the errors brought on by, theoretically, relatively incomplete resolution of particle detection techniques over particle species, velocities, and counts, and practically, spacecraft charging, make it inadequate to calculate current density and charge density using three-dimensional distribution functions of particles of all kinds. The sizable error in measuring current and charge densities are not inevitable, though, if one starts with the measurement of magnetic and electric field, which is far more precise. In this regard, the electric current is usually calculated with curlometer when a constellation of multiple spacecraft is available, rather than with $\sum_{\alpha} n_{\alpha} q_{\alpha} \mathbf{v}_{\alpha}$, the direct summation of electric currents over all kinds of carriers^[70]. Charge density, a quantity with a close relationship to electric current, is also preferable to calculate using Gauss's law^[71, 72],

$$\rho = \epsilon_0 E_{i,i}. \quad (1.4)$$

Although these multispacecraft missions fare very well in measuring current and charge densities, they are not prevalent in space exploration, in particular, the exploration into deep space where but one spacecraft is present. In such cases, direct measurement

technique has to be used to calculate electric current. This technique is less suitable to measure charge density than electric current which is usually larger and more observable. The charge density, due to the quasi-neutrality of plasmas, can be of six order less than that of particles' number density times the elementary charge. This point is evident from examining the one-dimensional Harris model^[73], in which the difference between proton and electron numbers is

$$n_p - n_e = -2n_0 \frac{V^2/c^2}{1 - V^2/c^2}, \quad (1.5)$$

and assuming the velocity V to be the speed of solar wind at 1au, which is roughly 400km/s. Therefore, it is helpful to develop a technique for single-spacecraft measurement that can be applied to measure charge density in space with high enough accuracy. One method is making four electric field measurement devices onboard, but this is not effective because the electric field is measured by six electric potential probes distributed along three orthogonal axes of the spacecraft frame, every two probes on one direction measuring the electric field along that direction.

A more fit solution is using potential measurements to directly deduce the charge density which is, essentially, a linear combination of the quadratic gradient components of the scalar potential field, as^[72]

$$\rho = -\epsilon \phi_{,i,i}. \quad (1.6)$$

The problem is how we can estimate the quadratic gradient from multipoint measurement.

1.3.2 On magnetic reconnection

Magnetic reconnection play important roles in many dynamical plasma processes in the solar system. For example, a series of solar activities, including prominence eruption^[74], solar flare^[75], and corona mass ejection^[76], are powered by and related to magnetic reconnection. It also, according to our current understanding^[77], make great contributions to the corona heating.

Similarly playing important roles in magnetic reconnection are the magnetic diffusion and dissipation that determine the magnetic reconnection rate. Without the diffusion term $\eta \nabla^2 \mathbf{B}$ in the magnetic induction equation,

$$\frac{\partial \mathbf{B}}{\partial t} = \nabla \times (\mathbf{V} \times \mathbf{B}) + \eta \nabla^2 \mathbf{B}, \quad (1.7)$$

the magnetic field lines are "frozen in" the plasmas, and no reconnection could possibly happen. The observational investigation of the diffusion process on magnetohydrodynamic scale entails the measurements of both the magnetic diffusivity, η , and the Laplacian of \mathbf{B} in the induction equation. It is easy to obtain the magnetic diffusivity, $\eta = 1/(\mu_0\sigma)$, which is defined using the electric resistivity that is readily calculated using Ohm's law based on the measurements of electric field and electric current from the MMS mission. The Laplacian involves the diagonal elements of the magnetic field's quadratic gradient that are currently achievable through three newly developed algorithms^[78–80] that take advantage of various physical constraints on the magnetic field and partial measurements to reduce the freedoms in the problem. We would like to construct a general algorithm that merely requires the measurements of the field itself as input and therefore can be applied to a multitude of scalar, vectorial, and tensor fields beyond magnetic fields.

1.3.3 On the torsion of magnetic field lines

The magnetic field line is the star on the stage of space. Its motion pulls plasma with it; its vibration excites Alfvén waves; its diffusion and dissipation are assigned with a big name, magnetic reconnection; its twist and shear trigger flares on the Sun. All the complex magnetic structures in space are, ultimately, composed of a bunch of bent and twisted magnetic field lines.

As a mathematical object, it is a three-dimensional curve whose local geometrical is completely determined by its curvature and torsion, one accounting for the curve's bending, the other accounting for its twisting. Therefore, in observational studies on various dynamical processes and static and transient magnetic structures in space, good knowledge about the magnetic field line's geometry, that is, a quantitative determination of its curvature and torsion is very beneficial for how, exactly, these processes and structures are related to the magnetic field's topology.

The curvature's estimation is achieved by MCA, as is discussed in Section 1.2. The estimation of the torsion have to build on the linear and quadratic gradients (LQGs) of the magnetic field. According to the torsion's definition,

$$\tau = \dot{\mathbf{N}} \cdot \mathbf{B}_n, \quad (1.8)$$

where \mathbf{N} is the normal of the curve, \mathbf{B}_n is the binormal, and a dot atop \mathbf{N} indicates a

directional derivative along the curve's arc length, the torsion of a magnetic field line can be deduced as^[78]

$$\tau = \frac{1}{\kappa^2} \epsilon_{ijk} b_i b_j b_k (b_m b_{n,m} b_{k,n} + b_m b_n b_{k,n,m}) , \quad (1.9)$$

where $\mathbf{b} = \mathbf{B}/B$ is the unit directional vector of the magnetic field. It is evident that we can estimate it only if the quadratic gradient of the magnetic unit vector is available.

1.4 The research contents of the dissertation

The main research contents of this dissertation are as follows:

- (1) we examine possible approaches to estimate the linear and quadratic gradients of physical fields.
- (2) we examine the application of Taylor's theorem and the least square method to the determination of the linear and quadratic gradients of physical fields using data acquired either simultaneously or non-simultaneously from different numbers of measurement points.
- (3) we, using computer simulation, investigate the feasibility, efficiency, reliability, and accuracy of the estimation of linear and quadratic gradients using one of the algorithms shown in the second part of this dissertation.

CHAPTER 2

GENERAL ALGORITHMS FOR THE LINEAR AND QUADRATIC GRADIENTS OF PHYSICAL FIELDS

2.1 Introduction

LQGs of physical fields play important roles in both dynamical and static processes involving electromagnetic fields and particles of all kinds and of all energy levels in space. A good grasp of these processes requires not only consistent observations of physical quantities in space which always appear as fields but also proper estimation and recording of the gradients of first order, second order, and even higher orders, of the physical fields observed. As is discussed in Section 1.2, the electric current, for example, is derived using curlometer technique which calculates the linear gradient of the magnetic field and obtains the electric current by summing relevant gradient components according to Ampère's circuital law^[81]. The torsion of a magnetic field line can only be attained by adding components of the quadratic gradient of the magnetic field^[78]. Analyzing these gradients of physical fields can help us gain more knowledge about physical phenomena in space. In this chapter, we review a recently proposed algorithm by Shen et al., ALQG^[82], that can estimate the spatial LQGs of physical fields using a set of more compact notation, and based on it develop a time-dependent algorithm that can estimate the temporo-spatial LQGs. The linear gradient achieved in this chapter is of higher-order accuracy than by a former algorithm derived by Harvey^[44].

The outline of this chapter is as follows. In Section 2.2, we introduce the basic theory of numerical differentiation which lays down the basis for the algorithm calculating the LQGs. In Section 2.3 we examine a naive application of the numerical differentiation technique introduced in Section 2.2, which is only for functions with one variable, or in other words for functions in one-dimensional space, on calculating the LQGs of a function with three variables, that is, a function in three-dimensional space. Section 2.4 gives a comprehensive review of ALQG using a set of more compact notation that can help it clarify. Section 2.4.1 presents the way ALQG combines Taylor's theorem and the method of least square to establish a set of estimating tensor equations of order up to four, which

should be consistently solved to attain the estimations of the LQGs. Section 2.4.2 shows a compact form of the estimating equations of ALQG, following which a detailed and comprehensive review on the physical meaning of each term of these equations is conducted and some advantages brought about by setting the geometric center as the target point of the algorithm are mentioned. Section 2.4.3 presents a brute method that solves the set of equations numerically when viewing them as a system of linear equations. Section 2.4.4 shows more of subtlety and in accord with the role of each term in the three tensor equations an approach that is applied by ALQG to solve the equations numerically. Add to that in Section 2.4.4 the review in Section 2.4.5 that deals with the tensor equation of highest order of the triplet completes the whole algorithm. In Section 2.4.6 we make a thorough discussion on two characteristic matrices that emerge from the solution of the tensor equation of the highest order and show great importance for their influence on the algorithm's truncation error. Section 2.5 give a mathematical proof to the statement in ALQG that at least ten measurement points are needed to conduct a calculation. Section 2.6 is devoted to developing an time-dependent algorithm for ALQG to stretch its ability to calculate the temporal LQGs and also make it go at poor clock synchronization among mountains of measurements. Section 2.7 is a summary and discussion of the constructions and findings in this chapter.

2.2 Basics of numerical differentiation

Numerical differentiation has been well developed for more than a hundred to two hundred years. The question soliciting it from mathematical giants in the 18th and 19th centuries is whether a derivative $f'(c)$ can be estimated from several known values of $f(x)$, such as $f(x_i)$ at x_i for $i = 1, 2, \dots, n$. The general answer is yes which is qualified by the development of various numerical differentiation techniques. The usual way to address this problem is to start from the definition of the derivative of a real function,

$$f'(x) = \lim_{h \rightarrow 0} \phi(x, h), \quad (2.1)$$

where $\phi(x, h) = (f(x + h) - f(x)) / h$ is equivalent to a single variable function $\phi_x(h)$ whose value is closer to $f'(x)$ when its variable h is closer to zero. In other words, the larger the value of h assumes, the greater the difference between $\phi(x, h)$ and $f'(x)$ goes.

Therefore, the function $\phi(x, h)$ can be used as an estimator of $f'(x)$ as

$$\tilde{f}'(x) = \frac{f(x+h) - f(x)}{h}. \quad (2.2)$$

Here we add a tilde atop the mathematical character f to indicate it is an estimation of f . When values of $f(x)$ at two points, say x_1 and x_2 , are extracted by some measurements on the real function, the derivative of it at the two points can be estimated as $\phi(x_1, x_2 - x_1)$ and $\phi(x_2, x_1 - x_2)$. In fact, these two estimations are equal because only one estimation can be obtained this way by taking into account function values at two points. This can be realized by combining

$$\begin{aligned} \tilde{f}'_2(x) &= \frac{f(x_2) - f(x)}{x_2 - x}, \\ \tilde{f}'_1(x) &= \frac{f(x_1) - f(x)}{x_1 - x}, \end{aligned}$$

to get

$$\tilde{f}'_1(x) + \left(\tilde{f}'_2(x) - \tilde{f}'_1(x) \right) \frac{x_2 - x}{x_2 - x_1} = \frac{f(x_2) - f(x_1)}{x_2 - x_1} \quad (2.3)$$

A general estimator of $f'(x)$ at any point x can then be set as

$$\tilde{f}'(x) = \frac{f(x_2) - f(x_1)}{x_2 - x_1} \quad (2.4)$$

As seen from the left-hand side of eq. (2.3), this estimator contains minor error when both $\tilde{f}'_2(x)$ and $\tilde{f}'_1(x)$ are good estimators and $|x_2 - x|$ not too larger than $|x_2 - x_1|$, which requires that x is close to both x_1 and x_2 .

To access the error contained in the estimator shown in eq. (2.2), Taylor's theorem is recalled. The theorem can be written as,

$$f(x+h) = f(x) + hf'(x) + \frac{h^2}{2}f''(\xi). \quad (2.5)$$

By comparing this equation with eq. (2.2), the error is readily obtained as $f''(\xi)h/2$ which converges to zero linearly with h . In the same way, the error involved in the general estimator that can evaluate the derivative of a real function at any point as shown in eq. (2.4), can be accessed by invoking Taylor's theorem twice as,

$$\begin{aligned} f(x+h_1) &= f(x) + h_1f'(x) + \frac{h_1^2}{2}f''(x) - \frac{h_1^3}{6}f'''(\xi), \\ f(x+h_2) &= f(x) + h_2f'(x) + \frac{h_2^2}{2}f''(x) - \frac{h_2^3}{6}f'''(\zeta), \end{aligned}$$

and combining them to get

$$f'(x) = \frac{f(x+h_1) - f(x+h_2)}{h_1 - h_2} - \frac{h_1 + h_2}{2} f''(x) + \mathcal{O}((h_1 - h_2)^2). \quad (2.6)$$

By comparing eq. (2.6) with eq. (2.4), the error is easily discerned as varying linearly with $h_1 + h_2$. A special case is $h_1 = -h_2 \equiv h$ when the second term on the right-hand side of eq. (2.6) vanishes and the error, therefore, is at the order of h^2 . This special estimator of higher accuracy while using the same information as input can be written explicitly as,

$$\tilde{f}'(x) = \frac{f(x+h) - f(x-h)}{2h}. \quad (2.7)$$

It is noted that the estimated derivative at the center point of the two measurement points is of the highest accuracy.

2.3 A rudimental consideration for simultaneous measurements

Since the total mass and volume of payloads onboard a spacecraft and the number of spacecraft in a fleet are highly restricted by the expensive launches of rockets, the making uses of multipoint measurement data acquired through space missions have to be to their limit. The geometric center is of this advantage when the derivative of a physical field at some point is to be calculated based on the data sampled at multiple locations. This is evidenced by the special case introduced in Section 2.2 that the estimator of eq. (2.7) gives an accuracy of one order higher than the general estimator of eq. (2.4) does.

A naive approach to calculate the linear gradient of a field is by applying eq. (2.7) three times on four measurements at four non-planar points. The points in a constellation of four in the following are tagged with both \mathbf{x}_α for themselves and $x_{\alpha i}$ in the form of their components. Here the Greek character $\alpha = 1, 2, 3, 4$ is the index of measurement point and the Latin character $i = 1, 2, 3$ is for the three spatial dimensions x, y, z . Estimations can then be derived as

$$\partial'_\beta \tilde{f}((\mathbf{x}_1 + \mathbf{x}_\beta)/2) = \frac{f(\mathbf{x}_1) - f(\mathbf{x}_\beta)}{|\mathbf{x}_1 - \mathbf{x}_\beta|}, \quad (2.8)$$

when the first measurement point, \mathbf{x}_1 , is chosen as the base point. Here $\beta = 2, 3, 4$ indicates the rest measurement points and ∂'_β indicate the partial differentiation along the direction of the vector $\mathbf{x}_1 - \mathbf{x}_\beta$. These estimations are of second-order accuracy.

However, a problem arises due to the detachment of three linear gradient components at three locations, $(\mathbf{x}_1 + \mathbf{x}_\beta) / 2$ for $\beta = 2, 3, 4$. To unite them at a single location, one may impose them upon the linear gradient components at the base position \mathbf{x}_1 . This is identical to applying eq. (2.2) instead of eq. (2.7) to the four measurements and gives first-order rather than second-order accuracy.

A simple way to calculate the quadratic gradient is to calculate the linear-gradient of the linear gradient. Building on four linear gradients calculated using data from four sets of four-point measurement, i.e. a sixteen-point measurement, the quadratic gradient can be obtained similarly as the linear gradients are obtained. This method, nonetheless, is not of interest, because it does not give an estimation with the least error, nor does it minimize the number of measurement points required to calculate the quadratic gradient. As we shall see shortly, the geometric center, in three-dimensional space as it in one-dimensional space, has merit to achieve the algorithm's minimal error. And merely ten points of measurement instead of sixteen are required to provide complete information of the quadratic gradient.

In summary, a simple application of the differential technique in one-dimensional space to the estimation of LQGs in space of higher dimensions fails.

2.4 The time-independent algorithm

A physical field is always a continuous function of space and time. In this section, we are interested in the field invariant in terms of temporal variable would make a comprehensive review on ALQG^[82], an algorithm that can calculate the spatial LQGs. As a convention for this section, since time is omitted, spatial LQGs are simply referred to by LQGs. To simplify the appearance of the algorithm, a scalar field f is used here in replacement for any tensor field that may concern the data analysts in real application, since a tensor field is composed of scalar fields.

There are ten degrees of freedom in the question of calculating the LQGs of the scalar field f at a given spatial point, say \mathbf{x} , one of which is for the field itself $f(\mathbf{x})$, three of which are for its linear-gradient components $\partial_i f(\mathbf{x})$ where $i = 1, 2, 3$, six of which are for its independent quadratic gradient components $\partial_i \partial_j f(\mathbf{x})$ where $i = 1, 2, 3$ and $j = 1, 2, 3$. Note that here we assumed $\partial_i \partial_j f(\mathbf{x}) = \partial_j \partial_i f(\mathbf{x})$ since physical fields are always infinitely

differentiable. To provide full information to estimate these ten eventual values, at least ten points of measurement are needed. This requirement is proved mathematically in Section 2.5, and also verified in the computer simulation shown in Chapter 3.

Taylor's theorem is a good start point to consider the question, but cannot lead to the end on its own right. A better approach is to combine it with mathematical optimization, that is, to minimize the error of the algorithm. The method of optimization has already been used by Harvey in deriving the algorithm for calculating the spatial linear gradient of a physical field based on four or more points measurement^[44]. But the author has not taken advantage of Taylor's theorem and hence that of the geometric center of measurement points. Independently, Shen et al. combined the Taylor's theorem and the least square method to construct the ALQG that can derive not only the linear gradient but also the quadratic gradient of a field at the center of measurement-point constellation.

2.4.1 Approximating in three-dimensional space

The general Taylor expansion of the scalar field $f(\mathbf{x}_0 + \Delta\mathbf{x})$ at point \mathbf{x}_0 reads,

$$f(\mathbf{x}_0 + \Delta\mathbf{x}) = f(\mathbf{x}_0) + \Delta x_i \partial_i f(\mathbf{x}_0) + \frac{1}{2} \Delta x_i \Delta x_j \partial_i \partial_j f(\mathbf{x}_0) + o(|\Delta\mathbf{x}|^2) \quad (2.9)$$

Let the positions of $N \geq 10$ measurement points be \mathbf{x}_α , $1 \leq \alpha \leq N$ and their displacement be $\Delta\mathbf{x}_\alpha$ from the target point, \mathbf{x}_0 , at which we wish to determine the LQGs of the field f , $\partial_i f(\mathbf{x}_0)$ and $\partial_i \partial_j f(\mathbf{x}_0)$, from the simultaneous measurement $f(\mathbf{x}_\alpha)$ at each measurement point α . To simplify the equation of Taylor expansion and the equations following, we introduce the notations of f_0 , $f_{0,i}$, $f_{0,i,j}$, where a comma in subscript indicates a partial differentiation, as substitutes for $f(\mathbf{x}_0)$, $\partial_i f(\mathbf{x}_0)$, and $\partial_i \partial_j f(\mathbf{x}_0)$, respectively, and also f_α for $f(\mathbf{x}_\alpha)$. eq. (2.9) can then be rewritten for measurement point α as,

$$f_\alpha = f_0 + \Delta x_{\alpha i} f_{0,i} + \frac{1}{2} \Delta x_{\alpha i} \Delta x_{\alpha j} f_{0,i,j} + o(|\Delta\mathbf{x}|^2). \quad (2.10)$$

The last term in eq. (2.10), $o(|\Delta\mathbf{x}|^2)$, is a truncation error and varies at higher than the second order of $|\Delta\mathbf{x}|$. If it vanishes, the resultant estimation of the ten values, \tilde{f}_α , $\tilde{f}_{0,i}$, and $\tilde{f}_{0,i,j}$, are precise. Here \tilde{f} with a tilde atop indicate that it is an estimation of the real value f . The greater the error is, the greater error would be contained in the estimated values. This is where optimization comes in, to minimize the error $o(|\Delta\mathbf{x}|^2)$.

By summing the squared error over all measurement point indices, we obtain the action, or total error, as

$$S = \frac{1}{N} \sum_{\alpha=1}^N \left(f_{\alpha} - \tilde{f}_0 - \tilde{f}_{0,i} \Delta x_{\alpha i} - \frac{1}{2} \tilde{f}_{0,i,j} \Delta x_{\alpha i} \Delta x_{\alpha j} \right)^2. \quad (2.11)$$

To obtain its minimum, we finely tune the values of the ten variables. Analytically, the fitted ten values can be achieved by solving a set of estimating equations which are derived by setting the action's partial differentiation with respect to the ten variables to be zero. These ten scalar equations can be cast into tensor forms and present as three tensor estimating equations,

$$\frac{\partial S}{\partial \tilde{f}_0} = 0, \quad \frac{\partial S}{\partial \tilde{f}_{0,k}} = 0, \quad \frac{\partial S}{\partial \tilde{f}_{0,k,l}} = 0. \quad (2.12)$$

It is noted that in the third tensor estimating equation which is for quadratic gradient, three more scalar equations that are duplicates of three in the six independent scalar equations, due to the symmetry of $\tilde{f}_{0,k,l}$, are included to make up the full nine-component tensor equation.

2.4.2 The estimating equations

The three tensor estimating equations in explicit forms are fairly tedious and weary. Before moving forward to solve them, we introduce new notations tackling the repetitions to simplify them and make their countenance more compact. Several quantities only related to the distribution of the constellation of measurement points are defined as,

$$R_i = \frac{1}{N} \sum_{\alpha=1}^N \Delta x_{\alpha i}, \quad (2.13)$$

$$R_{ij} = \frac{1}{N} \sum_{\alpha=1}^N \Delta x_{\alpha i} \Delta x_{\alpha j}, \quad (2.14)$$

$$R_{ijk} = \frac{1}{N} \sum_{\alpha=1}^N \Delta x_{\alpha i} \Delta x_{\alpha j} \Delta x_{\alpha k}, \quad (2.15)$$

$$R_{ijkl} = \frac{1}{N} \sum_{\alpha=1}^N \Delta x_{\alpha i} \Delta x_{\alpha j} \Delta x_{\alpha k} \Delta x_{\alpha l}. \quad (2.16)$$

Among them, R_i is the geometric center of the constellation, and R_{ij} is the volumetric tensor^[44]. Other quantities related both to the distribution of the constellation and to the

measured values of the field are defined as,

$$F = \frac{1}{N} \sum_{\alpha=1}^N f_{\alpha}, \quad (2.17)$$

$$F_i = \frac{1}{N} \sum_{\alpha=1}^N f_{\alpha} \Delta x_{\alpha i}, \quad (2.18)$$

$$F_{ij} = \frac{1}{N} \sum_{\alpha=1}^N f_{\alpha} \Delta x_{\alpha i} \Delta x_{\alpha j}. \quad (2.19)$$

The set of estimating equations in eq. (2.12) can thence be written explicitly as,

$$\tilde{f}_0 = F - \tilde{f}_{0,i} R_i - \frac{1}{2} \tilde{f}_{0,i,j} R_{ij}, \quad (2.20a)$$

$$\tilde{f}_{0,i} R_{ik} = F_k - \tilde{f}_0 R_k - \frac{1}{2} \tilde{f}_{0,i,j} R_{ijk}, \quad (2.20b)$$

$$\tilde{f}_{0,i,j} R_{ijkl} = c_{kl}, \quad (2.20c)$$

where

$$c_{kl} = 2 \left(F_{kl} - \tilde{f}_0 R_{kl} - \tilde{f}_{0,i} R_{ikl} \right), \quad (2.21)$$

is defined again for the reason of compactness and convenience. These equations involve the measured scalar field values contained in F s, i.e. F, F_i, F_{ij} , the configuration of the measurement constellation contained in R s, i.e. $R_i, R_{ij}, R_{ijk}, R_{ijkl}$, and the unknown field and its first-order and second-order partial derivatives at the point \mathbf{x}_0 to be estimated. The estimations can be acquired through solving this set of estimating equations.

To facilitate the process of solving eqs. (2.20a) to (2.20c), a good comprehension of each term of them is necessary. The first term on the right-hand side of eq. (2.20a), F , as defined by eq. (2.17) is the averaged measured field values which, in terms of perturbation theory, can be viewed as the zeroth approximation of the true field value we want to determine in the vicinity of the sites where data are drawn by the measurements. The second term, $\tilde{f}_{0,i} R_i$, involving the expansion displacement of first order, $\Delta x_{\alpha i}$, is the first-order perturbative correction to the zeroth term. And in the same way, the third term which contains squared expansion displacement, $\Delta x_{\alpha i} \Delta x_{\alpha j}$, is the second-order correction. Being added to by the first-order and second-order correction, the initial solution of the equation, or the zeroth approximation of the field value f_0 , becomes the second-order approximation containing decreased truncation error and therefore being of increased accuracy. In eq. (2.20b), the first term is the zeroth approximation of $f_{0,i} R_{ik}$. When the

equation does not contain the corrections of first order and second order following this term, it is presented in a similar form as derived by Harvey^[44] and by Shen et al.^[46] for the linear gradient of a field. Since we are pursuing the quadratic gradient as well as the linear gradient of a field, the corrections have to be retained in this equation. In the triad, the last tensor equation consisting of nine scalar equations, or six independent scalar equations, serves as a complement to the other two and furnish ranks in the whole system of the equations.

One thing that deserves a special mention before our diving into solving the equations is the importance of the geometric center of the constellation. As having been presented in Section 2.2, this point is of considerable account on reducing the error of and improving the accuracy of the estimation. In eqs. (2.20a) and (2.20b), the second term on the right-hand sides of the equal marks may vanish, since $R_i = 0$ for all i were the geometric center to be chosen as the target point \mathbf{x}_0 . Besides, the displacement of the Taylor expansion of eq. (2.10) may become the smallest ever available.

In spite of the great advantage the geometric center of the constellation brings about, here for the sake of the completeness and generality of the algorithm, the special target point is not chosen in replacement for the more general point \mathbf{x}_0 , and the terms containing R_i are kept in eqs. (2.20a) and (2.20b) as these equations stand.

2.4.3 Solving the estimating equations by linear system solvers

Now we turn to solving this complex and convoluted system of tensor equations of fourth order, that is, a set of tensor equations in which the highest order of the tensors involved reaches four.

One way to tackle it is by casting this system into the form of ten scalar linear equations containing ten unknowns. By arranging the ten unknown variables, $\tilde{f}_0, \tilde{f}_{0,i}, \tilde{f}_{0,i,j}$ into the vector in ten-dimensional vector space,

$$\mathbf{f} = \left(\tilde{f}_0 \quad \tilde{f}_{0,1} \quad \tilde{f}_{0,2} \quad \tilde{f}_{0,3} \quad \tilde{f}_{0,1,1} \quad \tilde{f}_{0,1,2} \quad \tilde{f}_{0,1,3} \quad \tilde{f}_{0,2,2} \quad \tilde{f}_{0,2,3} \quad \tilde{f}_{0,3,3} \right). \quad (2.22)$$

the system of linear equations, in matrix form, is

$$\mathfrak{F}_i = \mathfrak{R}_{ij} \mathbf{f}_j, \quad 1 \leq i, j \leq 10, \quad (2.23)$$

where the constant term is defined by

$$\mathfrak{F} = \left(F \quad F_1 \quad F_2 \quad F_3 \quad 2F_{11} \quad 2F_{12} \quad 2F_{13} \quad 2F_{22} \quad 2F_{23} \quad 2F_{33} \right), \quad (2.24)$$

and the coefficient matrix is defined as

$$\mathfrak{R} = \begin{pmatrix} 1 & R_1 & R_2 & R_3 & \frac{1}{2}R_{11} & R_{12} & R_{13} & \frac{1}{2}R_{22} & R_{23} & \frac{1}{2}R_{33} \\ R_1 & R_{11} & R_{21} & R_{31} & \frac{1}{2}R_{111} & R_{121} & R_{131} & \frac{1}{2}R_{221} & R_{231} & \frac{1}{2}R_{331} \\ R_2 & R_{12} & R_{22} & R_{32} & \frac{1}{2}R_{112} & R_{122} & R_{132} & \frac{1}{2}R_{222} & R_{232} & \frac{1}{2}R_{332} \\ R_3 & R_{13} & R_{23} & R_{33} & \frac{1}{2}R_{113} & R_{123} & R_{133} & \frac{1}{2}R_{223} & R_{233} & \frac{1}{2}R_{333} \\ 2R_{11} & 2R_{111} & 2R_{211} & 2R_{311} & R_{1111} & R_{1211} & R_{1311} & R_{2211} & R_{2311} & R_{3311} \\ 2R_{12} & 2R_{112} & 2R_{212} & 2R_{312} & R_{1112} & R_{1212} & R_{1312} & R_{2212} & R_{2312} & R_{3312} \\ 2R_{13} & 2R_{113} & 2R_{213} & 2R_{313} & R_{1113} & R_{1213} & R_{1313} & R_{2213} & R_{2313} & R_{3313} \\ 2R_{22} & 2R_{122} & 2R_{222} & 2R_{322} & R_{1122} & R_{1222} & R_{1322} & R_{2222} & R_{2322} & R_{3322} \\ 2R_{23} & 2R_{123} & 2R_{223} & 2R_{323} & R_{1123} & R_{1223} & R_{1323} & R_{2223} & R_{2323} & R_{3323} \\ 2R_{33} & 2R_{133} & 2R_{233} & 2R_{333} & R_{1133} & R_{1233} & R_{1333} & R_{2233} & R_{2333} & R_{3333} \end{pmatrix}. \quad (2.25)$$

Please note that eq. (2.20c) with two free indices k, l represent nine linear equations, among which six are independent since the equation is symmetric with respect to the two free indices, and correspond to the last six rows in \mathfrak{R} , or \mathfrak{R}_{ij} for $5 \leq i \leq 10, 1 \leq j \leq 10$. We may list in order the combinations of the two indices of the six independent equations as

$$\mathfrak{I} = \{k, l\}, \quad 1 \leq k \leq l \leq 3, \quad (2.26)$$

or explicitly,

$$\mathfrak{I} = \{\{1, 1\}, \{1, 2\}, \{1, 3\}, \{2, 2\}, \{2, 3\}, \{3, 3\}\}, \quad (2.26')$$

and based on it construct a six-dimensional linear space whose basis is

$$b_6 = \{\hat{\mathbf{k}}_M | 1 \leq M \leq 6\} = \{\hat{\mathbf{x}}_1\hat{\mathbf{x}}_1, \hat{\mathbf{x}}_1\hat{\mathbf{x}}_2, \hat{\mathbf{x}}_1\hat{\mathbf{x}}_3, \hat{\mathbf{x}}_2\hat{\mathbf{x}}_2, \hat{\mathbf{x}}_2\hat{\mathbf{x}}_3, \hat{\mathbf{x}}_3\hat{\mathbf{x}}_3\}. \quad (2.27)$$

This basis is in fact the basis of the last six dimensions of the ten-dimensional linear space in which resides eq. (2.23), which can be readily solved using common linear system solvers.

Using linear system solver is too brute to shed some light into the essence of the algorithm, and cannot give accuracy comparable to given by another method which is presented in Section 2.4.4. By this method, we could present a comprehensible and pedagogical way to address the problem in the form of tensor equations.

2.4.4 Solving the estimating equations by an iterative method

In light of the discussion in Section 2.4.2 on the meaning of the many terms in eqs. (2.20a) to (2.20c) with regard to perturbation theory, it is natural and reasonable to come up with an iterative method as the solver for the triad. This method is to produce one by one a sequence of approximation solutions that converge to the true solution. Supposing the approximation solution of k th order, the set of $\tilde{f}_0^{(k)}$, $\tilde{f}_{0,i}^{(k)}$, $\tilde{f}_{0,i,j}^{(k)}$, is obtained through computations beforehand, we substitute it into the right-hand side of eqs. (2.20a) to (2.20c) to calculate the corrections added to the zeroth approximation, such as F in eq. (2.20a) and F_k in eq. (2.20b), and compute a new version of the approximation solution on the left-hand side, that is, of $k + 1$ th order. Until an approximation solution with satisfactory accuracy is obtained, the computation of the method is not ceased. The first set of approximation solutions, or that of zeroth order, is usually improvised for the scalar field in real world to accelerate the computational convergence, or in other words, to reduce the number of iterations in computation. For simplicity, it is recommended to be set as zero, that is, $\tilde{f}_0^{(0)} = \tilde{f}_{0,i}^{(0)} = \tilde{f}_{0,i,j}^{(0)} = 0$.

Because the complexities involved in each of eqs. (2.20a) to (2.20c) are different, the time consumed in the computation for each equation varies. Computing them simultaneously and separately are not of advantage. In this case, it converges faster to the true solution when the computations are done consecutively, that is, to substitute the approximation of the LQGs of k th order, $\tilde{f}_{0,i}^{(k)}$, $\tilde{f}_{0,i,j}^{(k)}$, into eq. (2.20a) to obtain $\tilde{f}_0^{(k+1)}$, substitute the lately calculated $\tilde{f}_0^{(k+1)}$ and the old $\tilde{f}_{0,i,j}^{(k)}$ into eq. (2.20b) to obtain $\tilde{f}_{0,i}^{(k+1)}$, and substitute the newish $\tilde{f}_0^{(k+1)}$, $\tilde{f}_{0,i}^{(k+1)}$ into eq. (2.20c) to obtain $\tilde{f}_{0,i,j}^{(k+1)}$.

The step-by-step approach is summarized as follows for clarity,

- (1) Set the initial values of \tilde{f}_0 , $\tilde{f}_{0,i}$, and $\tilde{f}_{0,i,j}$.
- (2) Substitute current $\tilde{f}_{0,i}$ and $\tilde{f}_{0,i,j}$ into eq. (2.20a) to obtain a new \tilde{f}_0 .
- (3) Substitute current \tilde{f}_0 and $\tilde{f}_{0,i,j}$ into eq. (2.20b) to obtain a new $\tilde{f}_{0,i}$.
- (4) Substitute current \tilde{f}_0 and $\tilde{f}_{0,i}$ into eq. (2.20c) to obtain a new $\tilde{f}_{0,i,j}$.
- (5) Repeat steps 2-4 until a satisfactory accuracy of the estimation is achieved.

For Step (1), as has been discussed above, zeros are advised as the initial values. For Step (2), the computation is simple. For Step (3), with both sides of eq. (2.20b) multiplied by the inverse of the matrix R_{ij} , it is easy to calculate the new $\tilde{f}_{0,l}$ as

$$\tilde{f}_{0,l} = (R^{-1})_{kl} \left(F_k - \tilde{f}_0 R_k - \frac{1}{2} \tilde{f}_{0,i,j} R_{ijk} \right). \quad (2.28)$$

While the computations involved in eqs. (2.20a) and (2.20b) are straightforward, the task of solving eq. (2.20c) containing tensors of order as high as four to obtain $\tilde{f}_{0,i,j}$ is arduous and thereafter entails another special subsection devoted to it. In addition, the solution of this equation leads to some important insight into the capability of the algorithm.

2.4.5 Reducing tensor order

The form of eq. (2.20c), in general, is similar to that of eq. (2.20b). As an analogy to the solution of eq. (2.20b), eq. (2.20c) can be solved as a no-brainer when multiplied by the inverse of the fourth-order tensor R_{ijkl} , if there is one. But there is no method yet available to attain the inverse of a fourth-order tensor.

One thing noteworthy, if each term in the equation is inspected carefully, is that the indices i, j and k, l always appear as pairs. To put it another way, i always accompanies j and k always attend l . This point implies that we may combine the paired indices directly into one index and reduce the order of the tensor equation.

Let the index for the combination of indices (i, j) to be M and for (k, l) to be N . The original space on which eq. (2.20c) holds is three dimensional, and whose basis is the set of $(\mathbf{x}_1, \mathbf{x}_2, \mathbf{x}_3)$. After the combination, or transformation, since the fourth-order tensor R_{ijkl} is a fully symmetric tensor, the new space on which the transformed equation holds is six-dimensional, the basis of which is in actual fact eq. (2.27), the basis of the last six dimensions of the ten-dimensional linear space to which eq. (2.23) belongs.

Note that the transformed equation is not simply the eq. (2.20c) with subscripts substituted by M, N , because there are hidden summations over all three-dimensional indices that present twice as subscripts. A further work to be done is to transform these summations into their six-dimensional counterpart, that is, to convert $\sum_{i,j=1}^3$ to $\sum_{M=1}^6$ and $\sum_{k,l=1}^3$ to $\sum_{N=1}^6$. The summation over index M is identical to the summation $\sum_{i=1}^3 \sum_{j=i}^3$ as evidenced by the basis of the six-dimensional space shown in eq. (2.27). So eq. (2.20c)

may be rewritten as

$$\sum_{i=1}^3 \sum_{j=i}^3 (2 - \delta_{ij}) R_{ijkl} \tilde{f}_{0,i,j} = c_{kl}. \quad (2.29)$$

The coefficient, $2 - \delta_{ij}$, by which the left-hand side of the equation is multiplied, is a compensation to it for the lost terms of the exchange of i and j . The tensor R_{ijkl} is symmetric, but with the coefficient, $(2 - \delta_{ij}) R_{ijkl}$ is no longer symmetric with respect to (ij) and (kl) . To repair the broken symmetry, both sides of the equation is multiplied by one more coefficient, $(2 - \delta_{kl})$. Therefore, the equation reads

$$\sum_{i=1}^3 \sum_{j=i}^3 (2 - \delta_{kl})(2 - \delta_{ij}) R_{ijkl} \tilde{f}_{0,i,j} = (2 - \delta_{kl}) c_{kl}. \quad (2.30)$$

Now the subscripts indicating three-dimensional space can be replaced by the new set of indices of capitalized Latin characters, M, N which is for six-dimensional space, and the resultant equation reads

$$\tilde{\mathcal{F}}_M \mathcal{R}_{MN} = \mathcal{C}_N, \quad (2.31)$$

where

$$\mathcal{R}_{MN} = (2 - \delta_{kl})(2 - \delta_{ij}) R_{(ij)(kl)}, \quad (2.32)$$

$$\tilde{\mathcal{F}}_M = \tilde{f}_{0,i,j}, \quad (2.33)$$

$$\mathcal{C}_N = (2 - \delta_{kl}) c_{kl}. \quad (2.34)$$

Note that the \mathcal{R}_{MN} is symmetric because of the multiplication of $(2 - \delta_{kl})$, and only depends on the geometrical distribution of the measurement points since it is obtained from reducing R_{ijkl} 's order. It is a characteristic matrix of the distribution of the measurement points and, in fact, is of great significance as we shall see at the end of this subsection. The unknown vector \mathcal{F} comprises the exact six independent quadratic gradient components. The symmetric matrix \mathcal{R}_{MN} can be diagonalized and its the normalized eigenvectors corresponding to the eigenvalues $\lambda_M, 1 \leq M \leq 6$ with $\lambda_M \geq \lambda_N$ for all $M > N$, can be found as $b_{6e} = \{\hat{\mathbf{e}}_M | 1 \leq M \leq 6\}$. The transformation matrix from the basis of b_6 to b_{6e} , A_{MN} , is constructed by

$$\hat{\mathbf{e}}_M = A_{MN} \hat{\mathbf{k}}_N. \quad (2.35)$$

The coefficients of a vector, say $e_M \hat{\mathbf{e}}_M = k_M \hat{\mathbf{k}}_M$, on these two set of basis, are related by

$$e_M = k_N (A^{-1})_{NM}. \quad (2.36)$$

Since A^{-1} is the inverse of A , eq. (2.31) can be

$$\tilde{\mathcal{F}}_M (A^{-1})_{MJ} A_{JL} \mathcal{R}_{LK} (A^{-1})_{KO} A_{ON} (A^{-1})_{NI} = \mathcal{C}_N (A^{-1})_{NI},$$

where two sets of $A^{-1}A$ are inserted on the left-hand side and both sides are multiplied by a A^{-1} . Through straightforward calculation, this equation can be cast into the form comprising only coefficients of tensors on b_{6e} ,

$$F_I \lambda_I = C_I, \quad (2.37)$$

where $F_I = \mathcal{F}_M (A^{-1})_{MI}$ and $C_I = \mathcal{C}_N (A^{-1})_{NI}$ are the coefficients of the correspondent vectors in terms of the basis of b_{6e} . Note that the repetition of the index of I in this equation does not imply a summation convention. The unknown F_I is calculated by C_I/λ_I , and then through the inverse transformation from the basis of b_{6e} to b_6 can be converted to $\mathcal{F}_M = F_I A_{IM}$. This \mathcal{F} , according to eq. (2.33), is composed exactly of the six independent quadratic gradient components being looked for.

With eq. (2.20c) solved in this way, together with eqs. (2.20a) and (2.20b) solved in Section 2.4.4, a complete algorithm for LQGs of a physical field building on at least ten points measurement is established.

2.4.6 The characteristic matrices of the distribution of measurement points

The characteristic matrix \mathcal{R} and its relative, another characteristic matrix,

$$\mathcal{R}_{MN} = R_{(ij)(kl)}, \quad (2.38)$$

which is the directly reduced version of the fourth-order tensor R_{ijkl} are of great value on showing the capabilities and requirements of the algorithm and thereafter deserves some special comments before we leave this section. They rely on the distribution of the constellation and hence contain information about how the distribution affects the truncation error of the algorithm. But as defined with the tensor R_{ijkl} which depends on not only the constellation's distribution but also the position of the target point, they are not exactly intrinsic to the constellation. A better way to address this concern is to utilize the geometric center as the target point, and the corresponding tensors \mathcal{R}^c and \mathcal{R}^c for analysis.

At first glance, one may discern that the importance of \mathcal{R}^c lie in the fact that the eigenvalues of \mathcal{R}^c should not be zero, because otherwise the calculation of F_I using eq. (2.37) fails. To examine it in more detail, a direct relation between the number of zeros of its eigenvalues and the spatial configuration of the constellation is easily justified. When all measurement points are aligned along one direction, say x -axis, only Δx_1 does not vanish which lead to a bare R_{1111} survived and hence \mathcal{R}_{11}^c non-vanishing as,

$$\mathcal{R}^c = \begin{pmatrix} \mathcal{R}_{11}^c & 0 & \cdots \\ 0 & 0 & \cdots \\ \cdots & \cdots & \cdots \end{pmatrix}. \quad (2.39)$$

This is, in fact, the case of one non-zero and five zeros of the eigenvalues of \mathcal{R}^c . On the other hand, for measurement done on one line, no information about the difference of the physical field along two other directions orthogonal to it is obtained; And the LQGs cannot be calculated based on such measurements. When all measurement points are positioned in one single plane, intuitively, no gradient components along the normal of this plane can be obtained. Mathematically, supposing it is the plane of $x - y$, Δx_3 is zero, in which case all components of R with subscripts 3 are zeros, and only the up-left corner of the matrix \mathcal{R}^c has non-zero values as,

$$\mathcal{R}^c = \begin{pmatrix} \mathcal{R}_{11}^c & \mathcal{R}_{12}^c & \mathcal{R}_{13}^c & 0 & \cdots \\ \mathcal{R}_{21}^c & \mathcal{R}_{22}^c & \mathcal{R}_{23}^c & 0 & \cdots \\ \mathcal{R}_{31}^c & \mathcal{R}_{32}^c & \mathcal{R}_{33}^c & 0 & \cdots \\ 0 & 0 & 0 & 0 & \cdots \\ \cdots & \cdots & \cdots & \cdots & \cdots \end{pmatrix}. \quad (2.40)$$

This matrix's rank is three, so it can be diagonalized and with three non-zero eigenvalues left. The transformation of the basis in the diagonalization does not involve any unit vector in the six-dimensional space constructed upon the unit vector $\hat{\mathbf{x}}_3$ in three-dimensional space. So no information about the gradient along $\hat{\mathbf{x}}_3$ can be achieved which is consistent with the foregoing intuitive imagination.

Zeros of eigenvalues of the rank-deficient \mathcal{R}^c result in incalculable relevant F_I and therefore relevant components of $\tilde{\mathcal{F}}$. But small values of them, barely according to eq. (2.37), might not heavily affect the total error involved in the computation, for the reason that the error generated by the calculation of eq. (2.37) is a roundoff error that

is by several degrees smaller than the algorithm's truncation error. However, they may, through other ways, exert a strong influence on the total error, that is, by truncation error.

To get a more deep understanding of how the configuration of the constellation make an effect, rather than \mathcal{R}^c , it is more of goodness to dwell upon the characteristic matrix \mathcal{R}^c that is derived from reducing the order of the tensor R_{ijkl} directly without the multiplication by the coefficients $2 - \delta_{kl}$ and $2 - \delta_{ij}$. This is because \mathcal{R}^c is not a tensor, while \mathcal{R}^c is and its eigenvalues are invariant under the transformation of the coordinate system of the three-dimensional space. As a rule of thumb, invariants are always important quantities in physics. So do the eigenvalues of \mathcal{R}^c .

A comparison of this matrix with the volumetric tensor R_{ij}^c can be made to gain knowledge about what the eigenvalues of it stand for. In the case of calculating the linear gradient of a field, it is of particular interest to evaluate how far the constellation extends from its geometric center, because this distance, which may be referred to by l , determines the truncation error of the algorithm as the parameter h does for the estimator of eq. (2.7) in the one-dimensional case. To answer this question, we may construct a variance, along a certain direction \mathbf{n} , of the geometrically centric distances of all measurement points in the constellation as

$$\sigma^2(\mathbf{n}) = \frac{1}{N} \sum_{\alpha} (n_i \Delta x_{\alpha i})^2. \quad (2.41)$$

The standard deviation $\sigma(\mathbf{n})$ is assured of the quality the distance l has, since it is a measure of the dispersion of the measurement points' positions. However, $\sigma(\mathbf{n})$ is a function so variable with the direction \mathbf{n} that no specific value of it is set to be l . $\sigma(\mathbf{n})$ is bounded, so it has a maximum and a minimum along two directions perpendicular to each other. These two directions plus the third direction along which $\sigma(\mathbf{n})$ is stable can be obtained by subjecting the minimization problem to the constraint $\mathbf{n} \cdot \mathbf{n} = 1$, that is,

$$\frac{\partial}{\partial n_j} (\sigma^2(\mathbf{n}) + \lambda (\mathbf{n} \cdot \mathbf{n} - 1)) = 0, \quad (2.42)$$

or explicitly,

$$\frac{\partial}{\partial n_j} \left(\frac{1}{N} \sum_{\alpha} (n_i \Delta x_{\alpha i})^2 + \lambda (n_i n_i - 1) \right) = 0. \quad (2.43)$$

By distributing the partial differentiation to the two terms in the outmost parenthesis, this

equation is equivalent to

$$\frac{1}{N} \frac{\partial}{\partial n_j} \sum_{\alpha} (n_i \Delta x_{\alpha i})^2 + \lambda \frac{\partial}{\partial n_j} (n_i n_i - 1) = 0, \quad (2.44)$$

and further to

$$\frac{1}{N} \sum_{\alpha} n_i \Delta x_{\alpha i} \Delta x_{\alpha j} + \lambda n_j = 0. \quad (2.45)$$

This equation, by using the definition of R_{ij} in eq. (2.14), can be cast into a compact form,

$$R_{ji} n_i = \lambda n_j. \quad (2.46)$$

It is clear that \mathbf{n}_s , or \mathbf{n}_i for $1 \leq i \leq 3$, are the eigenvectors of the volumetric tensor R_{ji} . Along these directions, the maximal, median, minimal standard deviation of the distribution of the measurement points can be obtained as $\sigma(\mathbf{n}_i)$ for $1 \leq i \leq 3$. Since R_{ij} is symmetric, these eigenvectors are orthogonal. In the coordinates frame whose basis is the set of eigenvectors, \mathbf{n}_s , the matrix R_{ij} is diagonalized so as to make the remaining elements R_{ii} for $1 \leq i \leq 3$ to be the three eigenvalues λ_i , $1 \leq i \leq 3$ with $\lambda_i \geq \lambda_j$ for all $i > j$. And the three characteristic lengths, instead of a single length l that may not be appropriate for three-dimensional space, are exactly $l_i \equiv \sigma(\mathbf{n}_i) = \sqrt{R_{ii}} = \sqrt{\lambda_i}$. Therefore, the square roots of the three eigenvalues show the dispersion of the constellation along the three axes of its geometrically characteristic coordinates frame, and each, of l_i , serves as the small displacement h in eq. (2.7) for the corresponding direction, or dimension in three-dimensional space.

In the case of quadratic gradient, we conjecture that some characteristic parameter L_M for $1 \leq M \leq 6$ with $L_M \geq L_N$ for all $M > N$ takes similar effects, as l_i do in the linear gradient case, on the truncation error of the algorithm. Because differentiations are taken consecutively along two directions that are either orthogonal or identical to each other, the characteristic parameter may be in the form of $L_M = l_i l_j$ for $1 \leq i \leq 3, i \leq j \leq 3$. L_1 indicates the maximal variance of the constellation's distribution when combining the variances arising from two directions together. Note that the two directions may be the same, and intuitively, must be the same for the maximal and minimal variances. This point is plausible when one constructs a variance function as

$$\sigma^4(\mathbf{n}_1, \mathbf{n}_2) = \frac{1}{N} \sum_{\alpha} (n_{1i} \Delta x_{\alpha i})^2 (n_{2i} \Delta x_{\alpha i})^2. \quad (2.47)$$

If the form of the parameter, $L_M = l_i l_j$, exists, \mathcal{R}_{MN}^c should have, in quadratic gradient case, as has R_{ij} in linear gradient case, the role that its eigenvalues are directly related to the variance by $\sqrt{\mathcal{R}_{MM}^c} = L_M$. Its eigenvectors should be in the form of

$$\hat{\mathbf{e}}_M = \hat{\mathbf{x}}'_i \hat{\mathbf{x}}'_j, \quad (2.48)$$

where $\hat{\mathbf{x}}'_i = s_{ij} \hat{\mathbf{x}}_j$ are combinations of the basis vectors in three-dimensional space. Nonetheless, as we shall see in Chapter 3, eq. (2.48) does not necessarily hold, although $\hat{\mathbf{e}}_M$ are combinations of $\hat{\mathbf{k}}_M$ that are defined in terms of the basis of the three-dimensional space as in eq. (2.27).

2.5 Proof of the Required Number of Points at a Minimum

The fact that there are ten unknown variable altogether suggests ten measurements are needed. To prove this point, we may break it down to two parts and prove them separately. The first part is that there exists a set of ten measurements that can be used to estimate the complete linear and quadratic gradients. The second part is that any set of measurements less than ten cannot give a complete estimation based on the algorithm.

According to eq. (2.23), if the coefficient matrix \mathfrak{R} is of full rank, that is, ten, we can solve the equation to obtain the estimation. On the other hand, if \mathfrak{R} is not of full rank, in which case eq. (2.23) cannot have any unique solution, the estimation is not obtainable. Therefore, the two parts of the proof are transformed to that in the special case of ten measurements, \mathfrak{R} is of full rank, and that in any case of less than ten measurements, \mathfrak{R} is not a full rank matrix.

The first is easy to prove if we use some computer program to generate at random ten sets of three dimensional vectors, each representing in space the position at which a virtual measurement is made, and based on which the rank of \mathfrak{R} is calculated and compared with ten. The simulation regarding the error by number of measurement points shown in Section 3.5 is an example in which a set of ten positions makes full the rank of \mathfrak{R} and leads to complete and correct estimation.

The second part is a general proposition that requires more dedication. To prove the second part, we should consider another set of N estimation equations,

$$f_\alpha = \tilde{f}_0 + \Delta x_{\alpha i} \tilde{f}_{0,i} + \frac{1}{2} \Delta x_{\alpha i} \Delta x_{\alpha j} \tilde{f}_{0,i,j}, \quad (2.49)$$

where $1 \leq \alpha \leq N$.

We would like to show that eq. (2.20), or eq. (2.23), are linear combinations of eq. (2.49) over all possible α . Let E_α indicate eq. (2.49), and E_λ , $\lambda \in \{a, b, c\}$ for three equations of eq. (2.20). We have

$$\frac{1}{N} \sum_{\alpha} E_{\alpha} = E_a, \quad (2.50a)$$

$$\frac{1}{N} \sum_{\alpha} E_{\alpha} \Delta x_{\alpha\mu} = E_b, \quad (2.50b)$$

$$\frac{1}{N} \sum_{\alpha} E_{\alpha} \Delta x_{\alpha\mu} \Delta x_{\alpha\nu} = E_c. \quad (2.50c)$$

Therefore, eq. (2.20) or eq. (2.23) is a linear recombination of eq. (2.49) over all α . The coefficient matrices of these linear system are also subject to the same linear combination

$$\frac{1}{N} \sum_{\alpha} C_{\alpha j} = C_a = \mathfrak{R}_{1j}, \quad 1 \leq j \leq 10 \quad (2.51a)$$

$$\frac{1}{N} \sum_{\alpha} C_{\alpha j} \Delta x_{\alpha k} = C_b = \mathfrak{R}_{ij}, \quad 2 \leq k+2=i \leq 4, 1 \leq j \leq 10 \quad (2.51b)$$

$$\frac{1}{N} \sum_{\alpha} C_{\alpha j} \Delta x_{\alpha k} \Delta x_{\alpha l} = \mathfrak{R}_{ij}, \quad \{k, l\} \in \mathcal{I} \mapsto 5 \leq i \leq 10, 1 \leq j \leq 10 \quad (2.51c)$$

where C_α is the coefficient matrix of the linear system of eq. (2.49) as,

$$C_\alpha = \left(1, \Delta x_{\alpha i}, \frac{2-\delta_{ij}}{2} \Delta x_{\alpha i} \Delta x_{\alpha j} \right), \quad 1 \leq \alpha \leq 10, 1 \leq i \leq j \leq 3, \quad (2.52)$$

or explicitly,

$$C = \begin{pmatrix} 1, & \cdots, & 1 \\ \Delta x_{10}, & \cdots, & \Delta x_{100} \\ \vdots & \vdots & \vdots \\ \Delta x_{13}, & \cdots, & \Delta x_{103} \\ \frac{1}{2} \Delta x_{10} \Delta x_{10}, & \cdots, & \frac{1}{2} \Delta x_{100} \Delta x_{100} \\ \Delta x_{10} \Delta x_{11}, & \cdots, & \Delta x_{100} \Delta x_{101} \\ \vdots & \vdots & \vdots \\ \Delta x_{12} \Delta x_{13}, & \cdots, & \Delta x_{102} \Delta x_{103} \\ \frac{1}{2} \Delta x_{13} \Delta x_{13}, & \cdots & \frac{1}{2} \Delta x_{103} \Delta x_{103} \end{pmatrix}^T. \quad (2.52')$$

Note that on the right side matrix the superscript T represent transpose and 10 in the subscripts of the symbols in the last column of the matrix represents a single index rather than a combination of two indices 1 and 0. In eq. (2.51c), six combinations of k, l according to eq. (2.26) correspond to six possible value of the index $5 \leq i \leq 10$. eq. (2.51) can be rewritten as

$$(C_c)_{i\alpha} C_{\alpha j} = \mathfrak{R}_{ij}, \quad 1 \leq i, j \leq 10, \quad (2.53)$$

where the coefficient matrix C_c for the linear combination in eq. (2.50) as well as in eq. (2.51) is

$$(C_c)_\alpha = \begin{pmatrix} 1 \\ \Delta x_{\alpha k} \\ \Delta x_{\alpha k} \Delta x_{\alpha l} \end{pmatrix}, \quad 1 \leq \alpha \leq 10, 1 \leq k \leq l \leq 3, \quad (2.54)$$

or explicitly,

$$C_c = \begin{pmatrix} 1, & \cdots, & 1 \\ \Delta x_{10}, & \cdots, & \Delta x_{100} \\ \vdots & \vdots & \vdots \\ \Delta x_{13}, & \cdots, & \Delta x_{103} \\ \Delta x_{10} \Delta x_{10}, & \cdots, & \Delta x_{100} \Delta x_{100} \\ \Delta x_{10} \Delta x_{11}, & \cdots, & \Delta x_{100} \Delta x_{101} \\ \vdots & \vdots & \vdots \\ \Delta x_{12} \Delta x_{13}, & \cdots, & \Delta x_{102} \Delta x_{103} \\ \Delta x_{13} \Delta x_{13}, & \cdots, & \Delta x_{103} \Delta x_{103} \end{pmatrix}. \quad (2.54')$$

Note that 10 in the subscripts of the symbols in the last column represents a single index rather than a combination of two indices 1 and 0. According to eq. (2.53), we have

$$\text{rank}(\mathfrak{R}) \leq \min(\text{rank}(C_c), \text{rank}(C)). \quad (2.55)$$

The rank of C satisfy the inequality

$$\text{rank}(C) \leq \min(N, 10). \quad (2.56)$$

Combining eq. (2.55) and eq. (2.56), we get

$$\text{rank}(\mathfrak{R}) \leq N, \quad (2.57)$$

which means when the number of measurements is less than ten, $N < 10$, of eq. (2.23) the coefficient matrix, \mathfrak{A} , is not of full rank.

To this point where two parts of the original proposition that at least ten measurements are required to give complete estimation are proved successfully, we conclude this proposition true.

2.6 The time-dependent algorithm

The algorithm shown in Section 2.4 involves ten or more points measurement. If these points indicate instruments, such as electric potential probes onboard one spacecraft, it is easy to make sure that the measurements at different points are made simultaneously as is required by the time-independent algorithm shown in Section 2.4. For the case of multi points on multiple spacecraft, in which each instrument requires a spacecraft to carry it, the algorithm may require ten or more spacecraft to be temporally synchronized. This is not easily guaranteed in such a large constellation. To deal with the effect of poor satellite clock synchronization, a time-dependent algorithm is needed.

A complete description of a physical field in space and time is written, nominally, as $f(t, x, y, z)$ by extending the parameter space from three-dimensional space whose basis is solely spatial to four-dimensional space in which a vector \mathbf{x} has four components x_μ for $0 \leq \mu \leq 3$ standing for temporal and spatial parameters t, x, y, z . Note that Greek character is used as the component index for four-dimensional space here while Latin characters, as in Section 2.4, are used for three-dimensional space. A set of space-time parameters is sufficient to pinpoint a measurement. Multiple measurements conducted at different temporal and spatial positions by one spacecraft do not make any difference when compared with measurements by multiple spacecraft. In other words, using indices for the measurements is more accurate to distinguish the data input of the algorithm than for the spacecraft that performs the measurements. Therefore, we use \mathbf{x}_α for the temporal-spatial position where the measurement α is made and $x_{\alpha\mu}$ for the μ th component of the position.

The Taylor expansion of a field measurement f_α is written as

$$f_\alpha = f_0 + \Delta x_{\alpha\mu} f_{0,\mu} + \frac{1}{2} \Delta x_{\alpha\mu} \Delta x_{\alpha\nu} f_{0,\mu,\nu} + o(|\Delta \mathbf{x}|^2), \quad (2.58)$$

where Latin subscripts i, j in eq. (2.10) for time-independent measurements are replaced by Greek subscripts μ, ν for the time-dependent case. Note that α here is the index of

measurement rather than spacecraft.

The total error to be minimized, when N asynchronous measurements are conducted, is

$$S = \frac{1}{N} \sum_{\alpha=1}^N \left(f_{\alpha} - \tilde{f}_0 - \tilde{f}_{0,\mu} \Delta x_{\alpha\mu} - \frac{1}{2} \tilde{f}_{0,\mu,\nu} \Delta x_{\alpha\mu} \Delta x_{\alpha\nu} \right)^2, \quad (2.59)$$

which is again a simply extended version of its time-independent counterpart eq. (2.11).

With a similar approach to get eq. (2.12), fifteen scalar equations are obtained and kept in tensor form as

$$\frac{\partial S}{\partial \tilde{f}_0} = 0, \quad \frac{\partial S}{\partial \tilde{f}_{0,\mu}} = 0, \quad \frac{\partial S}{\partial \tilde{f}_{0,\mu,\nu}} = 0. \quad (2.60)$$

The first tensor equation in eq. (2.60) is a scalar equation. The second tensor equation is composed of four scalar equations as μ ranges from 0 to 3. The third tensor equation is the compact version of ten independent scalar equations since both μ and ν range from 0 to 3 and $\tilde{f}_{0,\mu,\nu}$ is symmetric with respect to μ and ν . Several quantities in close relationship with eqs. (2.13) to (2.16) that only depend on the temporal and spatial distribution of the constellation are constructed as follows

$$R_{\mu} = \frac{1}{N} \sum_{\alpha=1}^N \Delta x_{\alpha\mu}, \quad (2.61)$$

$$R_{\mu\nu} = \frac{1}{N} \sum_{\alpha=1}^N \Delta x_{\alpha\mu} \Delta x_{\alpha\nu}, \quad (2.62)$$

$$R_{\mu\nu\rho} = \frac{1}{N} \sum_{\alpha=1}^N \Delta x_{\alpha\mu} \Delta x_{\alpha\nu} \Delta x_{\alpha\rho}, \quad (2.63)$$

$$R_{\mu\nu\rho\sigma} = \frac{1}{N} \sum_{\alpha=1}^N \Delta x_{\alpha\mu} \Delta x_{\alpha\nu} \Delta x_{\alpha\rho} \Delta x_{\alpha\sigma}. \quad (2.64)$$

Note that α is the index for measurement points rather than four dimensions. R_{μ} is the spatial and temporal center of the measurements, and $R_{\mu\nu}$ is the volumetric tensor in four-dimensional space. Other quantities related both to the distribution of the constellation

and to the measured values of the field are defined similarly as,

$$F = \frac{1}{N} \sum_{\alpha=1}^N f_{\alpha}, \quad (2.65)$$

$$F_{\mu} = \frac{1}{N} \sum_{\alpha=1}^N f_{\alpha} \Delta x_{\alpha\mu}, \quad (2.66)$$

$$F_{\mu\nu} = \frac{1}{N} \sum_{\alpha=1}^N f_{\alpha} \Delta x_{\alpha\mu} \Delta x_{\alpha\nu}. \quad (2.67)$$

The set of estimating equations in eq. (2.60) can then be rewritten explicitly as,

$$\tilde{f}_0 = F - \tilde{f}_{0,\mu} R_{\mu} - \frac{1}{2} \tilde{f}_{0,\mu,\nu} R_{\mu\nu}, \quad (2.68a)$$

$$\tilde{f}_{0,\mu} R_{\mu\rho} = F_{\rho} - \tilde{f}_0 R_{\rho} - \frac{1}{2} \tilde{f}_{0,\mu,\nu} R_{\mu\nu\rho}, \quad (2.68b)$$

$$\tilde{f}_{0,\mu,\nu} R_{\mu\nu\rho\sigma} = c_{\rho\sigma}, \quad (2.68c)$$

where

$$c_{\rho\sigma} = 2 \left(F_{\rho\sigma} - \tilde{f}_0 R_{\rho\sigma} - \tilde{f}_{0,\mu} R_{\mu\rho\sigma} \right). \quad (2.69)$$

The methods of solving this set of time-dependent equations numerically are alike to those of solving time-independent equations, eqs. (2.20a) to (2.20c).

In general, there are two ways to solve them. The first, which is analogous to the method presented in Section 2.4.3 for time-independent case, is to cast this system of equations into fifteen independent linear equations in which fifteen unknown variables, \tilde{f}_0 , $\tilde{f}_{0,\mu}$ and $\tilde{f}_{0,\mu,\nu}$, can be obtained by solving them using linear system solvers. The explicit formation of this method is not presented here partly due to the bulky matrix of order 15×15 and partly for its similarity to its time-independent counterpart.

The other way, which is more of culture, as it not only iterates to refine the estimations of the unknown variables, which is the essence of the algorithm, but also make use of invariants internal to the distribution of the measurement points rather than the superficial components of the tensors, F s, and R s, is as same as presented in Section 2.4.4. The recommended procedure is as follows,

- (i) Set the initial values of \tilde{f}_0 , $\tilde{f}_{0,\mu}$, and $\tilde{f}_{0,\mu,\nu}$.
- (ii) Substitute current $\tilde{f}_{0,\mu}$ and $\tilde{f}_{0,\mu,\nu}$ into eq. (2.20a) to obtain a new \tilde{f}_0 .

- (iii) Substitute current \tilde{f}_0 and $\tilde{f}_{0,\mu,\nu}$ into eq. (2.20b) to obtain a new $\tilde{f}_{0,\mu}$.
- (iv) Substitute current \tilde{f}_0 and $\tilde{f}_{0,\mu}$ into eq. (2.20c) to obtain a new $\tilde{f}_{0,\mu,\nu}$.
- (v) Repeat steps 2-4 until a satisfactory accuracy of the estimation is achieved.

For Step (i), as has been discussed in Section 2.4.4, zeros are advised as the initial values. For Step (ii), the computation is simple. For Step (iii), with both sides of eq. (2.68b) multiplied by the inverse of the matrix $R_{\mu\nu}$, it is easy to calculate the new $\tilde{f}_{0,\sigma}$ as

$$\tilde{f}_{0,\sigma} = (R^{-1})_{\rho\sigma} \left(F_\rho - \tilde{f}_0 R_\rho - \frac{1}{2} \tilde{f}_{0,\mu,\nu} R_{\mu\nu\rho} \right). \quad (2.70)$$

To solve eq. (2.68c) and give a new estimation of $\tilde{f}_{0,\mu,\nu}$ based on current \tilde{f}_0 and $\tilde{f}_{0,\mu}$, it is again advisable to reduce the tensors' order and increase the dimension of the space from four to ten. Let the index for the combination of indices (μ, ν) to be Θ and for (ρ, σ) to be Σ . The new space constructed from the original four-dimensional space, whose basis is $(\hat{\mathbf{x}}_0, \hat{\mathbf{x}}_1, \hat{\mathbf{x}}_2, \hat{\mathbf{x}}_3)$, is ten-dimensional, the basis of which is

$$b_{10} = \{\hat{\mathbf{k}}_\Theta | 1 \leq \Theta \leq 6\} = \{\hat{\mathbf{x}}_0\hat{\mathbf{x}}_0, \hat{\mathbf{x}}_0\hat{\mathbf{x}}_1, \hat{\mathbf{x}}_0\hat{\mathbf{x}}_2, \hat{\mathbf{x}}_0\hat{\mathbf{x}}_3, \hat{\mathbf{x}}_1\hat{\mathbf{x}}_1, \hat{\mathbf{x}}_1\hat{\mathbf{x}}_2, \hat{\mathbf{x}}_1\hat{\mathbf{x}}_3, \hat{\mathbf{x}}_2\hat{\mathbf{x}}_2, \hat{\mathbf{x}}_2\hat{\mathbf{x}}_3, \hat{\mathbf{x}}_3\hat{\mathbf{x}}_3\}. \quad (2.71)$$

eq. (2.68c) in this ten-dimensional space reads

$$\tilde{\mathcal{F}}_\Theta \mathcal{R}_{\Theta\Sigma} = \mathcal{C}_\Sigma, \quad (2.72)$$

where

$$\mathcal{R}_{\Theta\Sigma} = (2 - \delta_{\rho\sigma})(2 - \delta_{\mu\nu}) R_{(\mu\nu)(\rho\sigma)}, \quad (2.73)$$

$$\tilde{\mathcal{F}}_\Theta = \tilde{f}_{0,\mu,\nu}, \quad (2.74)$$

$$\mathcal{C}_\Sigma = (2 - \delta_{\rho\sigma}) c_{\rho\sigma}. \quad (2.75)$$

The $\mathcal{R}_{\Theta\Sigma}$ is symmetric and only depends on the temporal and spatial distribution of the measurement points since it is obtained by the reduction of $R_{\mu\nu\rho\sigma}$'s order. It is a characteristic matrix of the distribution of the measurement points. The vector \mathcal{F} to be determined comprises the exact ten independent quadratic gradient components. The symmetric matrix $\mathcal{R}_{\Theta\Sigma}$ can be diagonalized and its the normalized eigenvectors corresponding to the eigenvalues $\lambda_\Theta, 1 \leq \Theta \leq 10$ with $\lambda_\Theta \geq \lambda_\Sigma$ for all $\Theta > \Sigma$, can be found as

$b_{10e} = \{\hat{\mathbf{e}}_\Theta | 1 \leq \Theta \leq 10\}$. The transformation matrix from the basis of b_{10} to that of b_{10e} , $A_{\Theta\Sigma}$, is constructed by

$$\hat{\mathbf{e}}_\Theta = A_{\Theta\Sigma} \hat{\mathbf{k}}_\Sigma. \quad (2.76)$$

The coefficients of a vector, $e_\Theta \hat{\mathbf{e}}_\Theta = k_\Sigma \hat{\mathbf{k}}_\Sigma$, on these two sets of basis, are related by

$$e_\Theta = k_\Sigma (A^{-1})_{\Sigma\Theta}. \quad (2.77)$$

By using the new basis, b_{10e} , for the ten-dimensional space, eq. (2.72) can be transformed into

$$F_\Upsilon \lambda_\Upsilon = C_\Upsilon, \quad (2.78)$$

where $F_\Upsilon = \mathcal{F}_\Theta (A^{-1})_{\Theta\Upsilon}$ and $C_\Upsilon = \mathcal{F}_\Sigma (A^{-1})_{\Sigma\Upsilon}$ are the coefficients of the correspondent vectors in terms of the basis of b_{10e} . The repetition of the index of Υ in this equation does not imply a summation convention. The unknown F_Υ is calculated by $C_\Upsilon/\lambda_\Upsilon$, and then through the inverse transformation from the basis of b_{10e} to b_{10} can be converted to $\mathcal{F}_\Theta = F_\Upsilon A_{\Upsilon\Theta}$. Step (iv) is worked out at this point.

By following the procedure from Step (i) to (v), one can calculate the LQGs of a scalar field in the four-dimensional space, that is, its space-time domain. In practice, the linear and quadratic gradient components involving the temporal domain, $f_{0,0}$ and $f_{0,0,i}$, are usually not of interest and hence can be disregarded. The ten other components that are solely spatial in this the time-dependent algorithm are obtained as the replacement for the ten concerning Section 2.4 in time-independent algorithm for a collection of data that are not well temporally synchronized.

This algorithm requires at least fifteen measurements as input. The five more measurements account for one more freedom added by the time derivative for the linear gradient, $f_{0,0}$, and four more freedoms for quadratic gradient by the combinations of a time derivative with itself and three spatial derivatives, $f_{0,0}$, $f_{0,1}$, $f_{0,2}$, $f_{0,3}$. A rigorous proof can be given in analogue to that, discussed in Section 2.5, of time-independent algorithm.

2.7 Summary and discussion

In this chapter, we reviewed a time-independent algorithm and building on it constructed a time-dependent algorithm for LQGs. The first is based on ten or more points

at which measurements are done simultaneously and therefore is time-independent. The other is based on fifteen or more measurements that scatter over not only spatial but also temporal domains which means it is time-dependent.

We first introduced the basics of numerical differentiation, which not only provided the foundation of the algorithm to be derived but also showed the good value of the geometric center as the target point of numerical differentiation in the one-dimensional case.

The first time-independent algorithm was introduced then. By making use of the Taylor's theorem that expressed the field at the measurement points which show no discrepancy in their time stamps as the field at the target point plus two small quantities involving LQGs and a truncation error, and the least square method that minimize the sum of squared truncation errors, a triad of tensor equations, or ten scalar equations, are constructed that gave estimations of the LQGs of a physical field at any target point not far from the constellation of measurement points. The time-independence of these equations requires that the measurements are conducted simultaneously which is easy to do for measurements on a single spacecraft and for measurements conducted on a small constellation of spacecraft. The geometric center is of particular interest when one is to achieve the highest accuracy available among those provided by the algorithm using all possible target points.

A brutal way to solve the set of equations is to view it as a system of linear equations whose coefficient matrix is of order 10×10 . The other way is to iterate over them in tensor forms, which is suggested by the fact that they are perturbative in nature. The procedure is summarized as five steps in Section 2.4.4. It is to calculate the field at the target point using predefined LQGs of it, then to calculate the linear gradient using the field and its predefined quadratic gradient, and after that to calculate the quadratic gradient using the obtained field and its linear gradient. This is the first iteration. The following iterations utilize the obtained field and its LQGs as predefined quantities and are performed until tidy accuracy is achieved. At least ten measurement points are required to fully determine the LQGs of the measured field, lest either the algorithms would collapse due to rank deficiency or the estimations would contain errors of considerable size even if the algorithms generate them in the usual ways.

Two characteristic matrices, \mathcal{R}^c and \mathcal{R} , appearing in the acquisition of quadratic gradient in the foregoing procedure play important role in the determination of the algorithm's truncation error. This is manifested both by the geometrical interpretation of their eigenvalues and by their comparison with the volumetric tensor which is long known for its influence on the linear gradient of a physical field^[44, 83]. The quadratic gradient can be estimated only if the six eigenvalues of the characteristic matrix \mathcal{R}^c are non-vanishing. \mathcal{R}^c is a variance of the constellation of measurement points along two directions as compared with the volumetric tensor as a variance along one direction.

A time-dependent algorithm was derived in a similar way as was for the time-independent case. In this scenario, different measurement data are not only distinguished by their spatial distribution but also temporal distinction. So this algorithm can be suitably applied to a large constellation of spacecraft, for which temporal synchronization is hard to achieve among its constituents. The spatial-temporal center of the measurements for this algorithm is of equal quality the geometric center has for the time-independent algorithm and is consequently recommended as the algorithm's target point. At the minimum, fifteen distinctive measurements are needed to give a sound estimation of the LQGs of the field.

The algorithm developed is general in that, except for the case of zero eigenvalues of the characteristic matrices, no severe restriction is imposed on the configuration of the constellation. As a constellation of spacecraft moves in space, each spacecraft proceeds along its own path, and the configuration, i.e. the shape, the size, and even more hidden features, of the constellation changes. The algorithm is robust under the ever-changing configuration. In addition, although the algorithm is developed above solely to estimate scalar physical fields, it is easily extended to estimate vector fields and even tensor fields of higher order as long as it is recognized that each component of a tensor field is a scalar field.

CHAPTER 3

TESTING THE TIME-INDEPENDENT ALGORITHM

3.1 Introduction

The two algorithms shown in Chapter 2 are able to estimate the LQGs of physical fields, when the measurements are done concurrently and non-concurrently, respectively. In this chapter, we focus on the modeling and test of the time-independent algorithm, which is the more basic algorithm. Our goal is to verify the feasibility and reliability of the algorithm and also test how its accuracy varies with the changing measurement conditions.

For measurements in the real world, the large-scale physical field we are interested in is always convoluted with fluctuations of short periods that are associated with wave disturbances. Various filters can be applied to eliminate all these fluctuations^[84], and thereafter prepare smooth data for the adequate application of our algorithm. In this regard, the data inputs of the algorithm in our modeling are set as free of noise and accurate. The sampling interval is another factor that would affect the overall accuracy and that comes before the involvement of the algorithm's truncation error. When the spatial sampling interval is comparable to the separation among measurement points, the algorithm fails because of undersampling which occurs when the sampling rate, which is the inverse of the sampling interval, is below the Nyquist rate which, in this case, is roughly the inverse of the spatial scale of the gradients. Since this is a limitation internal to multipoint measurement rather than to our algorithm, we make the data sampling instantaneous in the following modeling.

Using three magnetic field models and one electric potential model, we analyze the accuracy of the algorithm. The algorithm requires at least ten measurement points. In the following modeling, a fifteen-point measurement system is utilized to study the convergent behavior of the iteration method and the variation of the truncation error with relative measurement scale, L/D , which is the ratio of the measurement scale to the field structure scale, after which much more constellations consisting different numbers of measurement

points are included to explore the relationship between that number and the algorithm's truncation error.

In Section 3.2 we describe the constellation of the measurement points used for the modeling. In Section 3.3 we prove the feasibility and reliability of the algorithm and test its accuracy using a magnetic flux rope model. Section 3.4 shows the modeling of the algorithm to further calculate the curvature of magnetic field lines using a dipole magnetic field. In Section 3.5 by using a modeled magnetospheric field (MMF), we show the modeling to further calculate the torsion of magnetic field lines and also explore the relationship between the number of measurement points and the truncation error of the algorithm.

3.2 The configuration of the constellation

The modeling makes use of a constellation of fifteen spatial measurement points generated at random. In total, seventy-five numbers are generated randomly in the interval of $[0, 1)$, and grouped into fifteen sets of triads, each indicative of the three-dimensional coordinates, x, y, z , of a measurement point. The coordinates are then transformed into the geocentric reference system, that is, by subtracting the coordinates of the geometric center from each point's coordinates. The fifteen sets of coordinates are summarized in Tab. 3–1, in which α is the index of the measurement point. These points are also schematically shown in Fig. 3.1 which contains a three-dimensional view and two two-dimensional views. Note that the units of physical quantities in modeling are senseless, and therefore that units are omitted from not only the coordinates but magnetic field and electric potential field later on.

As had been discussed in Section 2.4.2, the geometric center of the constellation as the target point is of particular value to attain the highest accuracy. It also simplifies the calculation of the triad eqs. (2.20a) and (2.20b), since the vector R_i vanishes and two terms are thereafter omitted in these equations. For these two reasons, we choose it as the target point of the modeling that follows. And this is where the Δ ahead x, y, z in Tab. 3–1 comes in. $\Delta x, \Delta y$, and Δz are not merely the coordinates of each measurement point in the geocentric system but the distance of these points from the target point, as was defined in eq. (2.9).

Table 3–1: The distribution of the fifteen measurement points for time-independent algorithm's modeling.

α	$\Delta x_{(\alpha)}$	$\Delta y_{(\alpha)}$	$\Delta z_{(\alpha)}$
1	-0.35625871	0.31260078	-0.32278244
2	0.10122866	-0.34510246	-0.09863743
3	-0.0457695	0.05588475	-0.21706713
4	0.32933612	-0.24280729	0.04528155
5	0.12109147	0.51034979	-0.0619287
6	0.20122728	-0.30162608	-0.36376746
7	-0.40462318	-0.03405563	0.38863522
8	0.05050484	-0.1127686	-0.02729327
9	-0.04648151	-0.0895545	0.37713579
10	0.45307819	0.2590997	-0.27757502
11	0.14281801	0.47971461	0.01243332
12	-0.23975622	-0.27111845	0.38020116
13	0.19652825	0.14035597	0.29059016
14	-0.4270209	-0.07966877	-0.48569933
15	-0.07590281	-0.28130384	0.36047358

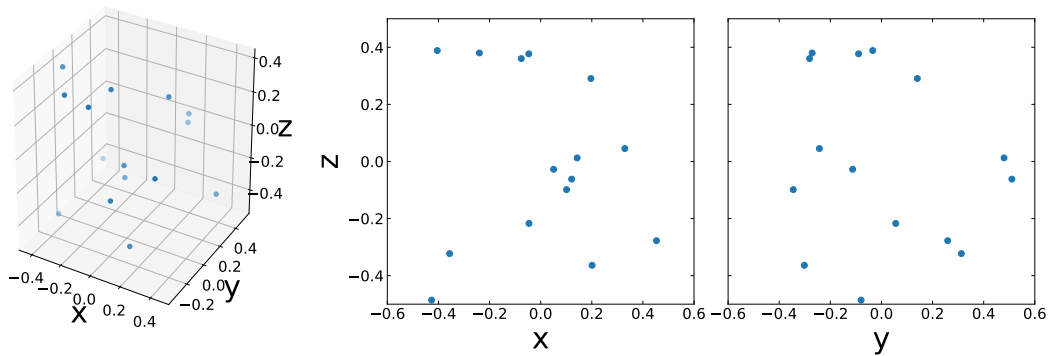


Figure 3.1: The distribution of the fifteen measurement points for time-independent algorithm's modeling.

Table 3–2: The eigenvalues of the characteristic matrix \mathcal{R}

λ_1	λ_2	λ_3	λ_4	λ_5	λ_6
0.002728	0.008468	0.01080	0.01130	0.02385	0.03512

The size of the constellation is of particular interest since it defines the measurement scale and hence the relative measurement scale. It, according to Harvey^[44], is twice the largest characteristic lengths of the constellation. The three characteristic length, the three square roots of the eigenvalues of volumetric tensor, of this constellation are $a = 0.75$, $b = 0.61$, and $c = 0.24$. So the size of it is $2a = 1.5$, and the measurement scale, by definition, is also $L \equiv 2a = 1.5$.

The characteristic matrix, \mathcal{R} , can be calculated based on the coordinates shown in Tab. 3–1 as

$$\mathcal{R} = \begin{pmatrix} 9.15 & 1.89 & -0.52 & 3.52 & -3.26 & 7.68 \\ 1.89 & 14.09 & -6.52 & 2.89 & -3.32 & 1.90 \\ -0.52 & -6.52 & 30.73 & -1.66 & 3.79 & 0.50 \\ 3.52 & 2.89 & -1.66 & 11.54 & -3.07 & 3.68 \\ -3.26 & -3.32 & 3.79 & -3.07 & 14.73 & -3.23 \\ 7.68 & 1.90 & 0.50 & 3.68 & -3.23 & 12.02 \end{pmatrix} \times 10^{-3}. \quad (3.1)$$

Its eigenvalues are shown in Tab. 3–2. They are not small values as compared with each element in the matrix of \mathcal{R} , which means the distribution is suitable for the algorithm. In the following modeling, the constellation's shape will remain unchanged when its size is scaled up and down so as to keep the relative positions of each point to others unchanged when adjusting the measurement scale of the constellation.

3.3 Magnetic flux rope

Magnetic flux rope is a basic magnetic structure that plays important roles in solar physics, heliophysics, and magnetospheric physics. So it serves as our first magnetic field model to test the algorithm. An axially symmetric, i.e. of zero oblateness, force free flux rope, according to Lundquist^[85], in cylindrical coordinates system reads

$$\mathbf{B} = B_0[0, J_1(\alpha r), J_0(\alpha r)], \quad (3.2)$$

where B_0 is the characteristic strength of the magnetic field of this model; J_n is the first kind of Bessel function of order n ; α is the reciprocal of the characteristic length in the $x - y$ plane of the flux rope; r is the distance between the observation point and the z -axis. Although how large the values of the overall magnetic strength and the spatial scale do not affect the accuracy analysis, for the sake of completeness, we formally set $B_0 = 60$ and $1/\alpha = 1$ in the modeling. Viewing the variation of the first kind Bessel functions of order zero and one with its variable, to set the characteristic structural scale $D = r$ when $r < 1$ and $D = 1$ when $r \geq 1$ is in order.

The linear gradient of a magnetic field is composed of 9 independent components, and the quadratic gradient of 18 components. They, in total, are composed of so many elements that detailed studies on each one are unnecessary. More over, repeated and redundant studies are so tedious that had better be simplified. Benefiting from the symmetries of the flux rope model, that the magnetic field is invariant both along the axial and along the azimuthal directions, we may reduce the number of components to deal with, since the linear gradient along these directions vanishes. It is of advantage to choose points on x -axis to be the geometric center of the constellation, as a straightforward contemplation on the variation of the field shows that, if so, only $B_{1,2}$, $B_{2,1}$, and $B_{3,1}$ for the linear gradient, and $B_{1,1,2}$, $B_{2,1,1}$, $B_{2,2,2}$, $B_{3,1,1}$, $B_{3,2,2}$ are non-vanishing, and the rest components are wiped out from the group. Without loss of generality by doing so, we can focus on analyzing truncation errors contained in estimations of non-vanishing components of a small band. More detailed surveys of all components of LQGs are deferred to the modeling using dipole magnetic field and MMF in Section 3.4 and Section 3.5.

We first investigate the algorithm's performance during iteration. In general, iteration methods do not necessarily lead to convergence. Even if the result of iteration is convergent, some require few iterations to achieve satisfactory results while others cost a huge price on calculation. Supposing the geometric center of the constellation shown in Tab. 3-1 is located at $[1, 0, 0]$ where the local field structure scale, D , is unit, we lower the distance among measurement points proportionally so as to reduce the size, i.e. the measurement scale L , of the constellation and hence the relative measurement scale to be $L/D = 0.026$. Iterative calculations using virtually measured magnetic field by this contracted constellation are then performed, during which the errors of the LQGs are kept

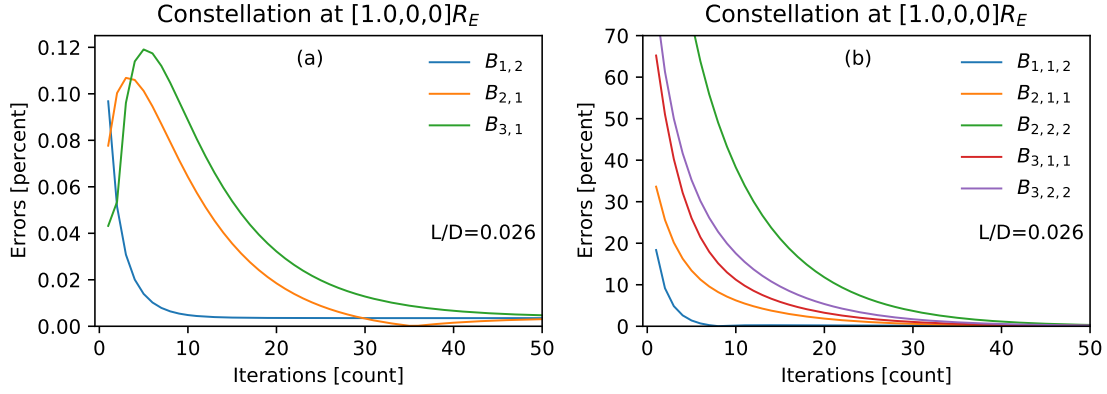


Figure 3.2: Relative errors of the non-vanishing components of the (a) Linear and (b) Quadratic magnetic gradients in the force-free flux rope computed by different numbers of iterations.

on record as shown in Fig. 3.2. The relative error (shown as the vertical axis) is defined as

$$\eta = \left| \frac{X_a - X_r}{X_r} \right|, \quad (3.3)$$

where X_a is the quantity obtained by the algorithm and X_r is its real value. The preset LQGs are null vector and null matrix respectively, meaning that the preset relative error is unit. By going through the first iteration (as shown along the horizontal axis), the relative errors contained in the three non-vanishing components of the linear gradient drop below 0.12%. By comparison, those of quadratic gradient remains high even though some component's error goes down to 10%. In the right half of each subfigure of Fig. 3.2, becomes more and more clear, as farther iterations are performed, certain almost fixed values to which the errors descend and converge steadily. These values are, in effect, the errors carried by the exact solutions of the system of eqs. (2.20a) to (2.20c). To reach an approximation solution that shows a manifest pattern of convergence, fifty iterations are needed in most cases despite the fickle nature of iterative methods. The calculation of the algorithm is fast in that three thousand iterations conducted by Python (numpy) using the Intel Core i5-6500 cost less than one second.

Second, we would like to study the reliance of the algorithm's accuracy on the relative measurement scale, L/D .

Intuitively, the accuracy would be higher when L/D is smaller. If the field consists of a lot of tiny structures whose scale is smaller than the measurement scale, this is, roughly the separation between measurement points, it is not even possible to give a poor estimation of the gradients at the geometric center. This point can also be acknowledged

by using mathematical formulation. Since D is defined as the characteristic scale of local field structure, it can be put in the form of

$$D \simeq f/|\nabla f|. \quad (3.4)$$

And L has the equivalent meaning of $|\Delta \mathbf{x}|$. The relative measurement scale is therefore

$$\frac{L}{D} \simeq \frac{L|\nabla f|}{f} \simeq \frac{|\Delta \mathbf{x}||\nabla f|}{f}. \quad (3.5)$$

The estimation of the gradients using Taylor's theorem eq. (2.9) fails when the corrective term is larger in terms of magnitude than the term to be corrected, i.e. $|\Delta \mathbf{x}||\nabla f| \geq f$. This point is also demonstrated by considering the perturbative nature of eqs. (2.20a) to (2.20c) and the behavior of iterative methods which no longer lead to convergence as long as L/D rise beyond a certain number that is close to unit.

The modeling is conducted by locating the geometric center of the constellation at $[1, 0, 0]$, $[0.5, 0, 0]$, and $[0.1, 0, 0]$ in Cartesian coordinates in a row. We increase and decrease the size of the constellation proportionally while keeping its shape to tailor measurement scale, L , for specified relative measurement scale L/D .

As shown in Fig. 3.3, reliable estimations are made by the algorithm for most L/D . Fig. 3.3a, 3.3c, and 3.3e show the errors of the estimated linear gradient (shown by solid lines) and thence the curvature (shown by dashed and dotted lines) of magnetic field lines of the force free flux rope magnetic field. In terms of value, they are generally below 5%, an low enough level of truncation error indicative of sound precision; In terms of trend, they show a dependence on the second order of L/D , which is proved by fitting using polynomial series. Fig. 3.3b, 3.3d, and 3.3f show the errors of the estimated quadratic gradient (shown by solid lines) and the torsion (shown by dotted lines) of magnetic field lines of the force free flux rope magnetic field. The relative errors of the quadratic gradient are below 5%, and that of the torsion calculated using the estimated gradients could be a little higher. These small relative errors shown in the modeling point to the reliability of the algorithm.

The magnetic field of the flux rope is, in a sense, a flattened structure in which no severe change in magnitude and direction occurs. This explains partly why it serves a highly effective and satisfactory model for testing, regarding the tidy accuracy achieved shown in Fig. 3.3. Nonetheless, magnetic structures in space may present steepness. For

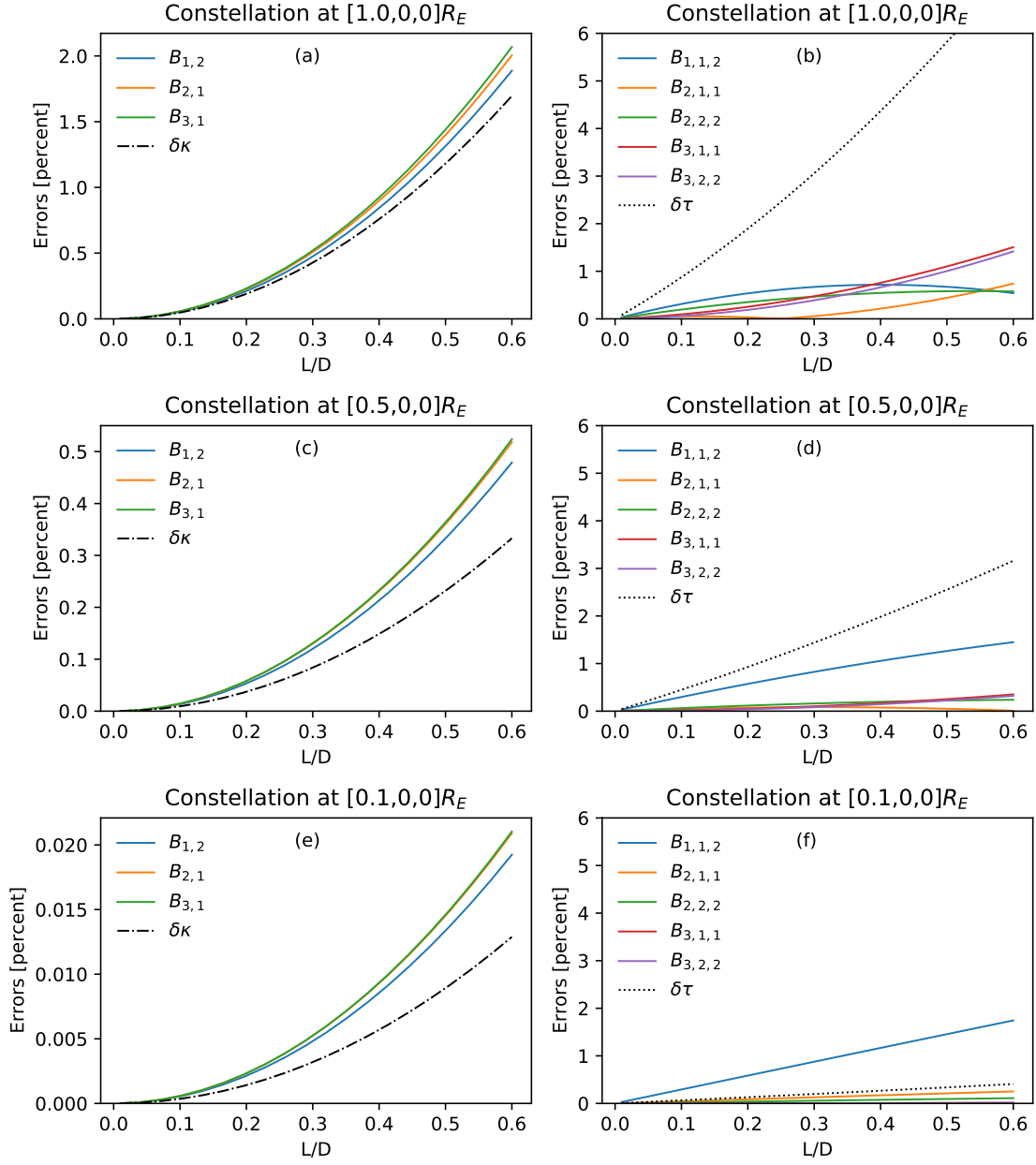


Figure 3.3: Relative errors in estimating the LQGs and curvature and torsion of the magnetic field lines of flux rope magnetic field by relative measurement scale. Panel (a) shows the relative errors in calculating the curvature of magnetic field lines and nonzero elements of the linear gradient of the force free magnetic flux rope field at $[1, 0, 0]$ in Cartesian coordinates. Panel (b) shows the relative errors in calculating the torsion of the magnetic field lines and nonzero elements of the quadratic gradient of the flux rope magnetic field at $[1, 0, 0]$. Panel (c) and (e) are similar to Panel (a) but for the flux rope magnetic field at $[0.5, 0, 0]$ and $[0.1, 0, 0]$ respectively. Panel (d) and (f) are similar to Panel (b) but for the flux rope magnetic field at $[0.5, 0, 0]$ and $[0.1, 0, 0]$ respectively.

example, the magnetic field of the inner magnetosphere is almost identical to a dipole field, which declines at the third order of r , the distance of the observation point from the dipole. This proportionality leads to, in Taylor expansion eq. (2.9), all the terms following the zeroth approximation on comparable order and hence low accuracy of the algorithm. In the following section, we would like to model the algorithm using a magnetic dipole field and prove yet again its feasibility and reliability.

3.4 Dipole magnetic field

The dipolar magnetic field in Cartesian coordinates is defined by

$$\mathbf{B} = \frac{M_3}{r^5} [3xz, 3yz, 3z^2 - r^2], \quad (3.6)$$

where M_3 is the strength of the magnetic dipole moment which is assumed to point at the positive z direction and $r = \sqrt{x^2 + y^2 + z^2}$ is the distance from the observation point to the dipole moment. We formally set $M_3 = 1$, as it is discussed in Section 3.3 that its value does not affect the relative truncation errors contained in estimations. The local spatial characteristic scale of the dipole magnetic field at the observation point, on account of eq. (3.4), is chosen as its distance from the dipole, where a factor of $1/3$ is dropped. The choice, mathematically, reads $D = r$.

We first, again, investigate the method's convergent trend during iterative calculations. The point of $[3, 0, 0]$ is of particular advantage to reduce the components of LQGs of the dipole field, and is chosen as the geometric center of the constellation. Only two components, $B_{1,3}$ and $B_{3,1}$, of the linear gradient, and five components, $B_{1,1,3}$, $B_{2,2,3}$, $B_{3,1,1}$, $B_{3,2,2}$, and $B_{3,3,3}$, among the eighteen independents of the quadratic gradient are non-vanishing. $L/D = 0.026$ is achieved for this modeling by adjusting the interspace among the measurement points.

Fig. 3.4a and 3.4b show the convergent trend of the LQGs of the magnetic dipole field. In general, the behavior of these relative errors is similar to that shown in Fig. 3.2 for the modeling using flux rope magnetic field. They converge within fifty iterations. The component $B_{1,1,3}$ in Fig. 3.4b shows a different pattern that the errors decrease at first and increase afterward. The errors for $B_{3,2,2}$ and $B_{2,2,3}$ have in addition to the decreasing and increasing the third stage, another decreasing. These are normal for iterative method which do not guarantee a monotonic converging. The intermediate values during itera-

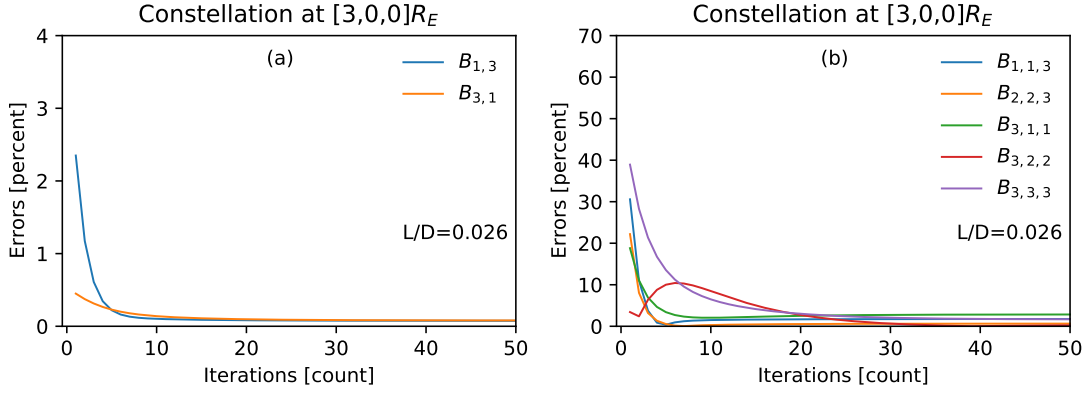


Figure 3.4: Relative errors of the non-vanishing components of the (a) Linear and (b) Quadratic gradients of magnetic dipole field computed by different numbers of iterations.

tions may fluctuate but will converge to the final value which is the true solution of the equation. This true solution, in our case, is not necessarily the true value of the estimated quantities, because the small quantities, $o(|\Delta \mathbf{x}|^2)$ in Taylor expansion of various measurements, are omitted through truncation in eq. (2.11). Therefore, the intermediate values may approximate the true value at first but fail to stick to it when moving toward the true solution of the truncated estimating equations.

We then calculate the LQGs and the curvature of magnetic field lines of the dipole magnetic field and test the algorithm for exponentially increasing relative measurement scales. The modeling is conducted by locating the geometric center of the constellation at $[3, 0, 0]$, $[2, 0, 3]$, and $[0, 0, 3]$ in Cartesian coordinates successively. We increase and decrease the size of the constellation proportionally while keeping its shape to tailor measurement scale, L , for specified relative measurement scale L/D .

Fig. 3.5a, 3.5c, and 3.5e show the relative truncation error in the estimations of the curvature (dash-dotted black line) of magnetic field lines and nonzero elements of the linear gradient (solid colored lines) of the magnetic dipole field. The theoretical curvature at $[0, 0, 3]$ is zero, so there is no line for it in Fig. 3.5c. As evidenced by the similarity between the solid black lines which varies at the second order of L/D and other lines, and also by polynomial fitting not shown in the figure, these linear gradients and curvatures are of second-order accuracy. The errors of linear gradient components are generally below 5% when $L/D < 0.1$.

Fig. 3.5b, 3.5d, and 3.5f show the relative truncation error in the estimations of

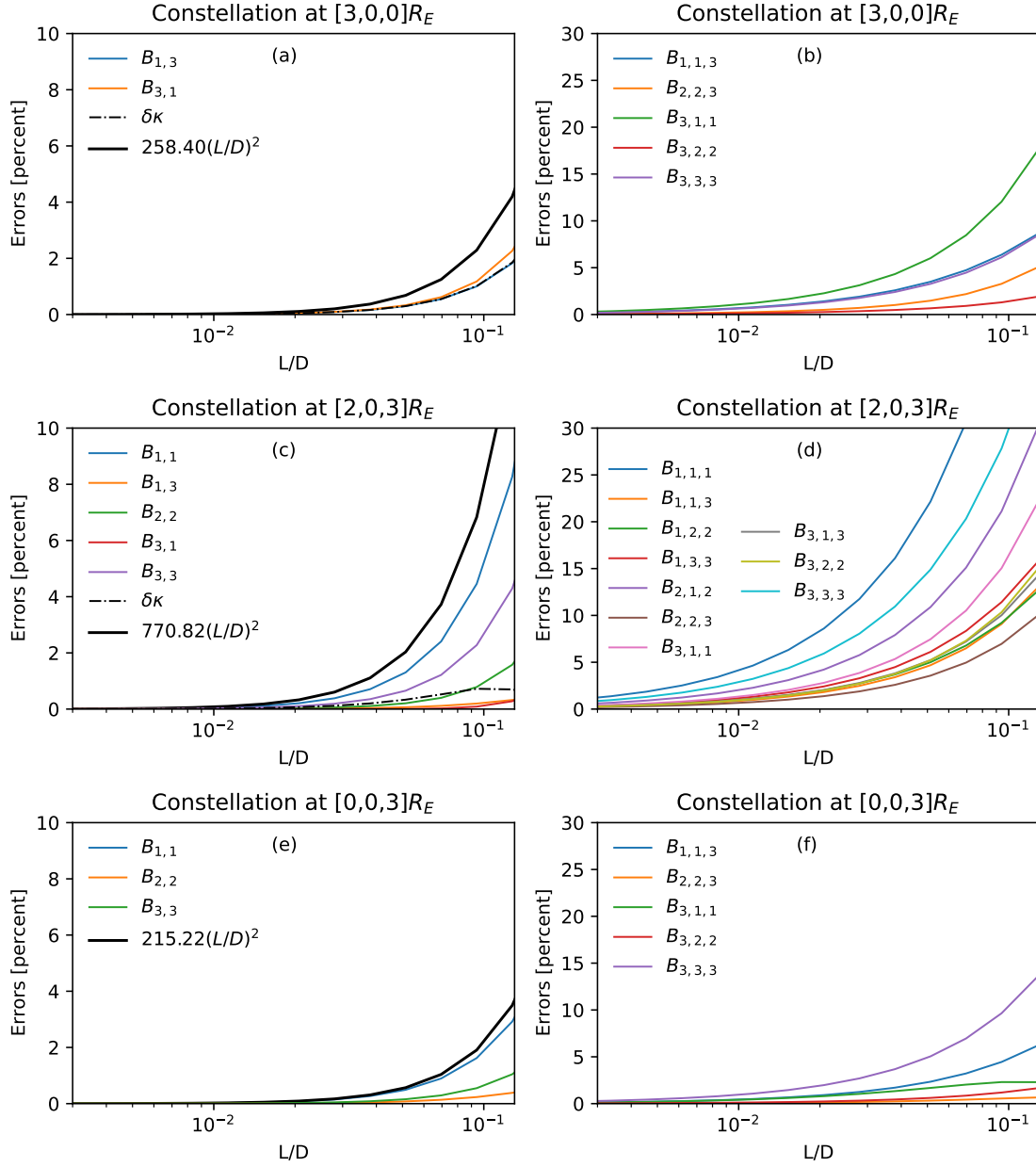


Figure 3.5: Relative errors in estimating the LQGs and curvature of the magnetic field lines of dipole magnetic field by relative measurement scale. Panel (a) shows the relative errors in calculating the curvature (dash-dotted black line) of magnetic field lines and nonzero elements of the linear gradient (solid colored lines) of the magnetic dipole field at $[3, 0, 0]$ in Cartesian coordinates. The solid black line is an example of function varying at the second order of L/D . Panel (b) shows the relative errors in calculating the nonzero elements of the quadratic gradient (solid colored lines) of the flux rope magnetic field at $[3, 0, 0]$. Panel (c) and (e) are similar to Panel (a) but for the flux rope magnetic field at $[2, 0, 3]$ and $[0, 0, 3]$ respectively. Panel (d) and (f) are similar to Panel (b) but for the flux rope magnetic field at $[2, 0, 3]$ and $[0, 0, 3]$ respectively.

the nonzero elements of the quadratic gradient (solid colored lines) of the magnetic dipole field. Since the filed lines are planar curves, the torsion of them is zero, i.e. $\tau = 0$. Therefore, there is no line for torsion in these subfigures. The quadratic gradients are of first-order accuracy. The errors are generally below 5% when $L/D < 0.01$.

A magnetic dipole is not able to produce complex magnetic field lines, which is indicated by the vanishing torsion. A more realistic model for the geomagnetospheric magnetic field is constructed by adding the field produced by one more mirrored dipole to the Earth's dipole field. A test of the algorithm using this model is described in the next section.

3.5 Modeled magnetospheric field

The MMF is defined as

$$\mathbf{B} = \frac{M_{z1}}{r_1^5}[3xz, 3yz, 3z^2 - r_1^2] + \frac{M_{z2}}{r_2^5}[3(x-40)z, 3yz, 3z^2 - r_2^2], \quad (3.7)$$

where two terms of the right side of the equation stand for the magnetic fields produced by two magnetic dipoles. The separation between them is 40 along the x -axis. Note that here units are omitted as they do not matter, and that R_E should be the unit of length in this formula if units are needed. The first dipole, whose moment is M_{z1} , is located at the origin of the coordinates system. $r_1 = \sqrt{x^2 + y^2 + z^2}$ is the distance from the observation point to the first dipole; And $r_2 = \sqrt{(x-40)^2 + y^2 + z^2}$ is that to the second dipole. The magnetic field lines are plotted in Fig. 3.6. The inner part of this field, or the inner magnetospheric field, is almost identical to a simple dipole field, while the outer region exhibits more complexity. So points far from the inner region are of advantage to test the algorithm under complex conditions. We utilize $[-5, 15, 10]$, $[5, 10, 10]$, and $[5, 15, 5]$ as the geometric center in the following modeling.

eq. (3.7) defines so asymmetric a field that any component of the LQGs of it is not null. These components stretch over so many orders which heavily convolves that some small components are severely affected by others of large value. Components of small value are usually of a lower level of merit for the exploration of physics in space and should be thought little of or even neglected. However, the relative error defined by eq. (3.3) barely differentiates between them. A better definition of the relative errors of

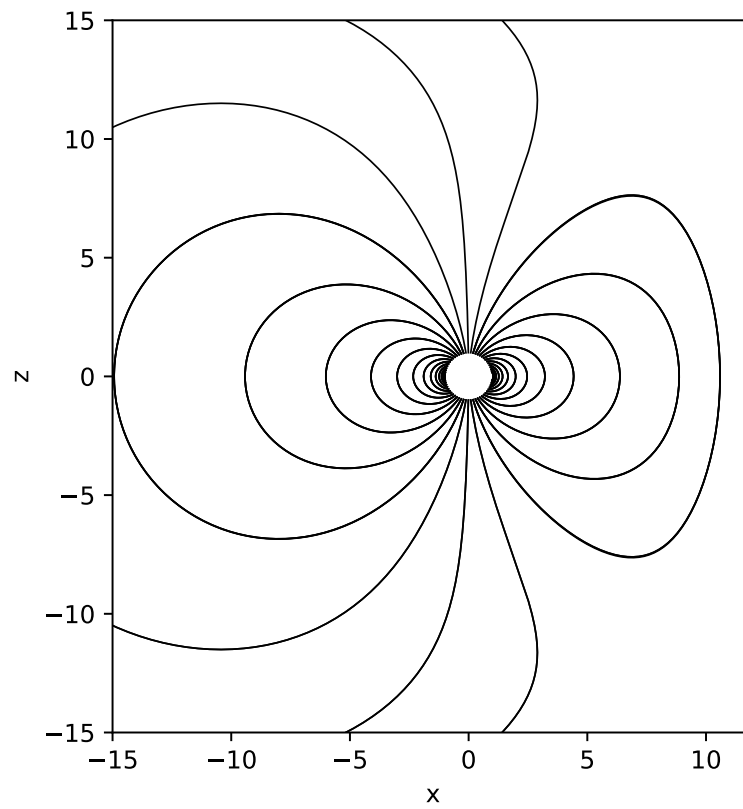


Figure 3.6: Magnetic field lines of the MMF in the $x - z$ plane.

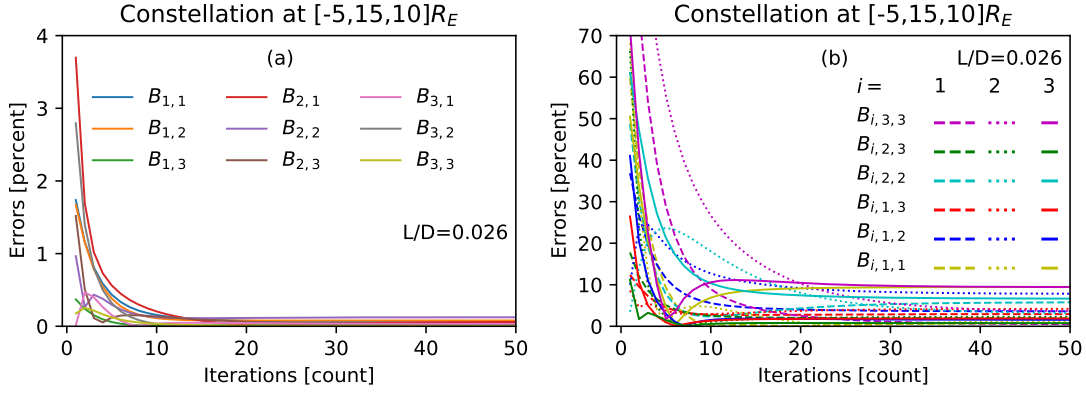


Figure 3.7: Relative errors of the non-vanishing components of the (a) Linear and (b) Quadratic gradients of the MMF computed by different numbers of iterations.

the LQGs will be

$$eta_{ij} = \frac{(B_{i,j})_a - (B_{i,j})_r}{\sum_{i,j}^3 |B_{i,j}|}, \quad (3.8)$$

and

$$eta_{ijk} = \frac{(B_{i,j,k})_a - (B_{i,j,k})_r}{\sum_{i,j,k}^3 |B_{i,j,k}|}. \quad (3.9)$$

Fig. 3.7a and 3.7b show the convergent behavior of the LQGs of the MMF within fifty iterations. The relative measurement scale is set to be $L/D = 0.026$ and the geometric center of the constellation is $[-5, 15, 10]$. It points to the feasibility and reliability of the algorithm for complex field structures in space.

Fig. 3.8a, 3.8c, and 3.8e show the relative truncation error in the estimations of the curvature (dash-dotted black line) of magnetic field lines and nonzero elements of the linear gradient (solid colored lines) of the magnetic dipole field. As evidenced by the similarity between the solid black lines which varies at the second order of L/D and other lines, and also by polynomial fitting not shown in the figure, these linear gradients and curvatures are of second-order accuracy. The errors of linear gradient components are generally below 5% when $L/D < 0.1$.

Fig. 3.8b, 3.8d, and 3.8f show the relative truncation error in the estimations of the torsion (dotted black line) of the magnetic field lines and nonzero elements of the quadratic gradient (solid colored lines) of the magnetic dipole field. The quadratic gradients are of first-order accuracy. The errors are generally below 5% when $L/D < 0.01$. The modeled truncation errors of the algorithm using MMF is akin to that using dipole magnetic field.

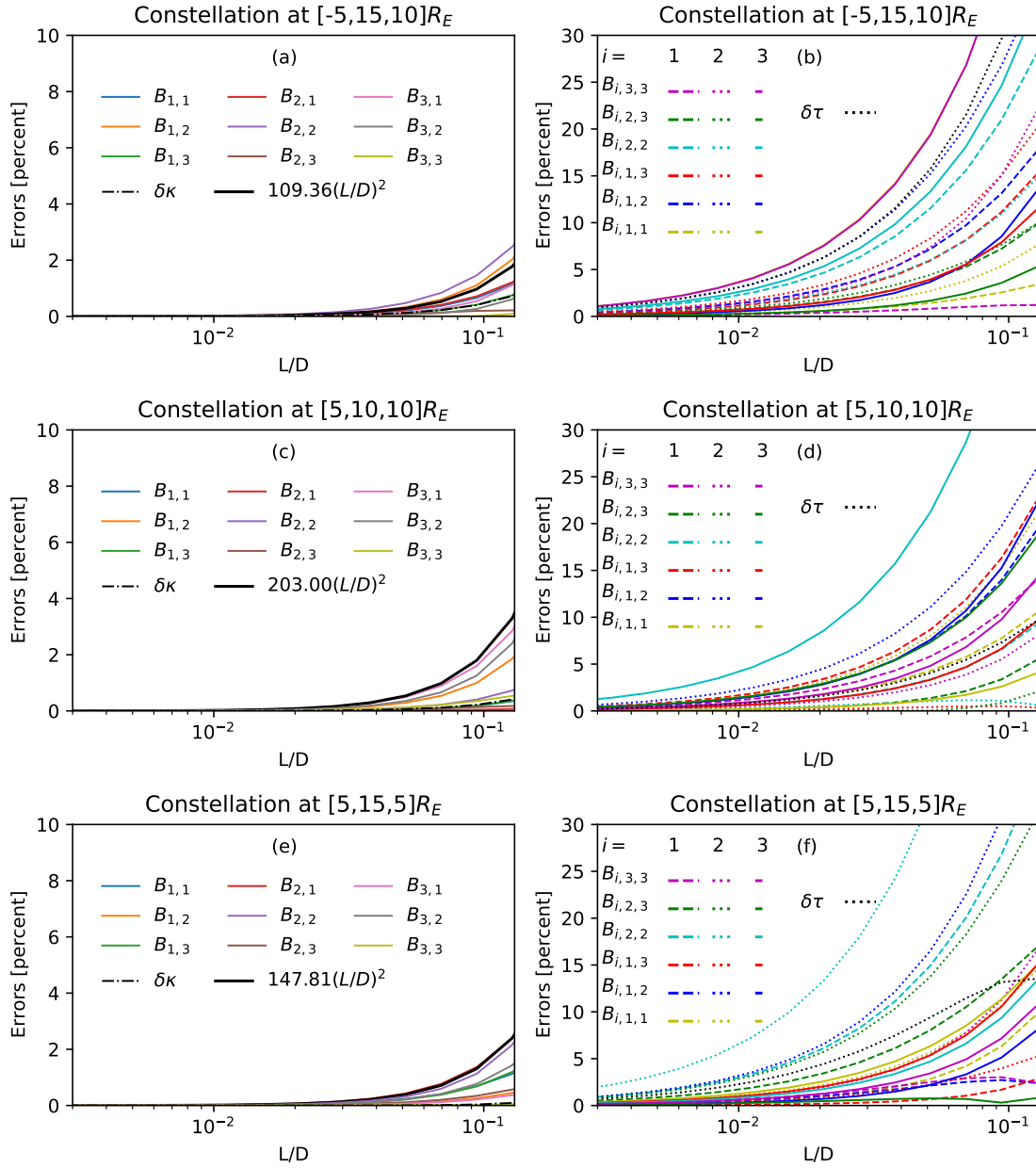


Figure 3.8: Relative errors in estimating the LQGs and curvature and torsion of the magnetic field lines of MMF by relative measurement scale. Panel (a) shows the relative errors in calculating the curvature of magnetic field lines and nonzero elements of the linear gradient of the MMF at $[-5, 15, 10]$ in Cartesian coordinates. Panel (b) shows the relative errors in calculating the torsion of the magnetic field lines and nonzero elements of the quadratic gradient of the magnetic field at $[-5, 15, 10]$. Panel (c) and (e) are similar to Panel (a) but for the magnetic field at $[5, 10, 10]$ and $[5, 15, 5]$ respectively. Panel (d) and (f) are similar to Panel (b) but for the magnetic field at $[5, 10, 10]$ and $[5, 15, 5]$ respectively.

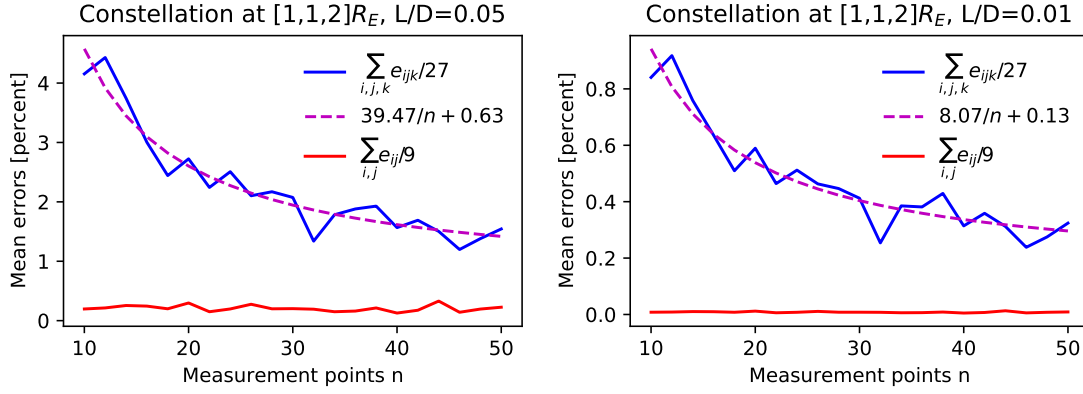


Figure 3.9: Averaged relative errors of estimating LQGs of the MMF by different number of measurements. The left panel shows the averaged relative errors for $L/D = 0.05$. The right panel shows the averaged relative errors for $L/D = 0.01$. The dashed magenta curve is inversely proportional to n .

In Section 3.3, Section 3.4, and this section, we have confirmed the reliability of the algorithm using fifteen-point measurement modeling. Intuitively, the algorithm could yield better results were more measurements included in the calculation. The exact relation between the accuracy and the number of measurement points can be modeled.

Since we are to investigate the algorithm's performance using measurement points of different number, the effect from the shapes of these points should be eliminated. To this end, we test the algorithm using one thousand randomly generated n -point constellations, the one that yields the least error of which is chosen as the delegate of the constellation of n -point measurement. By fixing L/D and the observation point, as usual, we make n the only variable.

Fig. 3.9a shows the variation of averaged relative errors contained in the estimations of the LQGs, $\sum_{i,j} \eta_{ij}/9$ and $\sum_{i,j,k} \eta_{ijk}/27$, at $[1, 1, 2]$ in the MMF for $L/D = 0.05$. The averaged error contained in the quadratic gradient's estimation is inversely proportional to n . And that for linear gradient's estimation is a constant. In the worst case, when only ten measurement points are available, the averaged error for the quadratic gradient is roughly 4%.

Fig. 3.9b shows the result of the modeling utilizing the same setup, except for a fixed $L/D = 0.01$. The plot is similar to the previous one. The only discernable difference is that the averaged error for the quadratic gradient is five times smaller, which is yet another sign of the errors' linearity on L/D .

3.6 Summary and discussion

In this chapter, we simulated the algorithm using force free magnetic flux rope, dipole magnetic field, and MMF, and confirmed its reliability and accuracy.

We first introduced a randomly generated constellation of fifteen measurement points. In the modeling that followed, virtually measured data are extracted at these places when its center was fixed to some target point its size was enlarged or contracted to meet a given relative measurement scale.

The simulations using all the three magnetic field models show the convergence under fifty iterative calculations. The estimations to which the calculations converged are accurate to second order for the linear gradient and to first order for the quadratic gradient. For the linear gradient, the overall truncation error is below 5% as the relative measurement scale is lower than 0.1, and for the quadratic gradient, it is below 5% as the relative measurement scale is lower than 0.01.

The simulation using the modeled magnetospheric field shows that the truncation error of the quadratic gradient is conversely related to the number of measurement points, that is, the more measurement points a constellation consists of, the higher accuracy the algorithm could achieve. However, this relation does not apply to the estimation of the linear gradient, the relative errors contained in which does not show dependency on the number of measurement points.

In summary, the time-independent algorithm shows considerable efficiency, robustness, and accuracy with regard to estimating the LQGs of manifold physical fields in space with at least ten measurement points.

CONCLUSIONS

In this dissertation, we systematically investigate the approaches to estimate the linear and quadratic gradients of physical fields, discuss an algorithm, ALQG, tackling time-independent joint measurements and develop a general algorithm tackling joint measurements spanning a temporal period, and confirm the time-independent algorithm's feasibility, reliability, and accuracy by simulations.

In Chapter 1, we introduce the history and the existing state of the measurement in space physics exploration. We briefly discussed the current applications of multipoint measurement techniques and other physical quantities to be measured in the future. In Chapter 2 and Chapter 3, we make contributions to the study of multipoint measurement and space physics exploration as summarized in what follows.

The main contribution of this dissertation can be concluded into the following three main parts.

- (1) This work analyzes possible approaches to construct the algorithms that can estimate the linear and quadratic gradients of physical fields and find that a proper combination of Taylor's theorem and the least square method can lead to the end.
- (2) This work reviews a general numerical time-independent algorithm for the linear and quadratic gradients of physical fields based on at least ten temporally synchronized measurements, and point to the importance, of two characteristic matrices of the constellation of measurement points, and of one special target point, the geometric center of the constellation, in determining the algorithm's accuracy.
- (3) This work develops a general numerical time-dependent algorithm for the linear and quadratic gradients of physical fields based on at least fifteen temporally discrepant measurements.
- (4) This work confirms the great efficiency, strong robustness, and high accuracy of the time-independent algorithm by testing it using three magnetic field models, force free magnetic flux rope, dipole magnetic field, and modeled magne-

tospheric field, find the quadratic dependence of linear gradient and the linear dependence of quadratic gradient on relative-measurement scale, and discovers the reciprocal relation between the truncation error contained in the algorithm's estimation and the number of measurement points.

The work in this dissertation is, by and large, not complete, because the time-dependent algorithm is not yet tested due the limited time available until the dissertation is written. I would conducted the test during my PhD period.

The time-independent algorithm, as its efficiency, robustness and accuracy have been proved, could find wide applications in the real world. One could be to determine the geometry of the magnetic disturbance field using AMPERE data and hence relate its configuration and variation to the sources that may have a great contribution. Another could analyze the measurements of the magnetic field made at a great number of magnetometer ground stations on the surface of the Earth.

REFERENCES

- 1 Gilbert W. De Magnete[M]. [S.l.] : Dover Publications, 2012.
- 2 Buick T. Astronomers' Universe : Orrery: A Story of Mechanical Solar Systems, Clocks, and English Nobility[M]. 1st ed. [S.l.] : Springer-Verlag New York, 2014.
- 3 Akasofu S-I, Chapman S. The ring current, geomagnetic disturbance, and the Van Allen radiation belts[J/OL]. Journal of Geophysical Research, 1961, 66(5) : 1321-1350. <http://dx.doi.org/10.1029/JZ066i005p01321>.
- 4 Meng X, Tsurutani B T, Mannucci A J. The Solar and Interplanetary Causes of Superstorms (Minimum Dst \leq -250 nT) During the Space Age[J/OL]. Journal of Geophysical Research: Space Physics, 2019, 124(6) : 3926-3948. <http://dx.doi.org/10.1029/2018JA026425>.
- 5 Acero F J, Vaquero J M, Gallego M C, et al. A Limit for the Values of the Dst Geomagnetic Index[J/OL]. Geophysical Research Letters, 2018, 45(18) : 9435-9440. <http://dx.doi.org/10.1029/2018GL079676>.
- 6 Carlowicz M. Storms from the sun : the emerging science of space weather[M]. Washington, DC : Joseph Henry Press, 2002.
- 7 Lanzerotti L J, Suess S T, Balogh A. The Heliosphere through the Solar Activity Cycle[M/OL]. [S.l.] : Springer Berlin Heidelberg, 2007. https://www.ebook.de/de/product/15973981/louis_j_lanzerotti_steve_t_suess_a_balogh_the_heliosphere_through_the_solar_activity_cycle.html.
- 8 Cameron R H, Schüssler M. Understanding Solar Cycle Variability[J/OL]. The Astrophysical Journal, 2017, 843(2) : 111. <http://dx.doi.org/10.3847/1538-4357/aa767a>.
- 9 Hathaway D H. The Solar Cycle[J/OL]. Living Reviews in Solar Physics, 2015, 12(1). <http://dx.doi.org/10.1007/lrsp-2015-4>.

- 10 Ichimoto K, Kubota J, Suzuki M, et al. Periodic behaviour of solar flare activity[J/OL]. *Nature*, 1985, 316(6027): 422-424. <http://dx.doi.org/10.1038/316422a0>.
- 11 Shimojo M, Yokoyama T, Asai A, et al. One Solar-Cycle Observations of Prominence Activities Using the Nobeyama Radioheliograph 1992-2004[J/OL]. *Publications of the Astronomical Society of Japan*, 2006, 58(1): 85-92. <http://dx.doi.org/10.1093/pasj/58.1.85>.
- 12 Webb D F, Howard R A. The solar cycle variation of coronal mass ejections and the solar wind mass flux[J/OL]. *Journal of Geophysical Research: Space Physics*, 1994, 99(A3): 4201. <http://dx.doi.org/10.1029/93JA02742>.
- 13 Curto J J. Geomagnetic solar flare effects: a review[J/OL]. *Journal of Space Weather and Space Climate*, 2020, 10: 27. <http://dx.doi.org/10.1051/swsc/2020027>.
- 14 Le G, Cai Z, Wang H, et al. Solar cycle distribution of great geomagnetic storms[J/OL]. *Astrophysics and Space Science*, 2011, 339(1): 151-156. <http://dx.doi.org/10.1007/s10509-011-0960-y>.
- 15 Chu X, McPherron R L, Hsu T-S, et al. Solar cycle dependence of substorm occurrence and duration: Implications for onset[J/OL]. *Journal of Geophysical Research: Space Physics*, 2015, 120(4): 2808-2818. <http://dx.doi.org/10.1002/2015JA021104>.
- 16 Kozyra J U, Valladares C E, Carlson H C, et al. A theoretical study of the seasonal and solar cycle variations of stable aurora red arcs[J/OL]. *Journal of Geophysical Research: Space Physics*, 1990, 95(A8): 12219. <http://dx.doi.org/10.1029/JA095iA08p12219>.
- 17 Burger R A, Kruger T P J, Hitge M, et al. A Fisk-Parker Hybrid Heliospheric Magnetic Field with a Solar-Cycle Dependence[J/OL]. *The Astrophysical Journal*, 2008, 674(1): 511-519. <http://dx.doi.org/10.1086/525039>.
- 18 Szabo A, Larson D, Whittlesey P, et al. The Heliospheric Current Sheet in the Inner Heliosphere Observed by the Parker Solar Probe[J/OL]. *The Astrophysical Journal*

- Supplement Series, 2020, 246(2): 47. <https://doi.org/10.3847/1538-4365/ab5dac>.
- 19 McComas D J, Elliott H A, Schwadron N A, et al. The three-dimensional solar wind around solar maximum[J/OL]. *Geophysical Research Letters*, 2003, 30(10): n/a-n/a. <http://dx.doi.org/10.1029/2003GL017136>.
- 20 Heber B. Modulation of galactic and anomalous cosmic rays in the inner heliosphere[J/OL]. *Advances in Space Research*, 2001, 27(3): 451-460. [http://dx.doi.org/10.1016/S0273-1177\(01\)00083-7](http://dx.doi.org/10.1016/S0273-1177(01)00083-7).
- 21 Upton L A, Hathaway D H. An Updated Solar Cycle 25 Prediction With AFT: The Modern Minimum[J/OL]. *Geophysical Research Letters*, 2018, 45(16): 8091-8095. <http://dx.doi.org/10.1029/2018GL078387>.
- 22 Pesnell W D, Schatten K H. An Early Prediction of the Amplitude of Solar Cycle 25[J/OL]. *Solar Physics*, 2018, 293(7). <http://dx.doi.org/10.1007/s11207-018-1330-5>.
- 23 Sarp V, Kilcik A, Yurchyshyn V, et al. Prediction of solar cycle 25: a non-linear approach[J/OL]. *Monthly Notices of the Royal Astronomical Society*, 2018, 481(3): 2981-2985. <http://dx.doi.org/10.1093/mnras/sty2470>.
- 24 ALLEN J A V, LUDWIG G H, RAY E C, et al. Observation of High Intensity Radiation by Satellites 1958 Alpha and Gamma[J/OL]. *Journal of Jet Propulsion*, 1958, 28(9): 588-592. <http://dx.doi.org/10.2514/8.7396>.
- 25 Li W, Hudson M. Earth's Van Allen Radiation Belts: From Discovery to the Van Allen Probes Era[J/OL]. *Journal of Geophysical Research: Space Physics*, 2019, 124(11): 8319-8351. <http://dx.doi.org/10.1029/2018JA025940>.
- 26 Chapman S, Ferraro V C A. A new theory of magnetic storms[J/OL]. *Journal of Geophysical Research*, 1931, 36(2): 77. <http://dx.doi.org/10.1029/TE036i002p00077>.

-
- 27 Cahill L J, Amazeen P G. The boundary of the geomagnetic field[J/OL]. *Journal of Geophysical Research*, 1963, 68(7): 1835-1843. <http://dx.doi.org/10.1029/JZ068i007p01835>.
- 28 Pfaff R F, Borovsky J E, Young D T. *Measurement Techniques in Space Plasmas: Fields*: Vol 103[M]. [S.l.]: American Geophysical Union, 1998.
- 29 Pfaff R F, Borovsky J E, Young D T. *Measurement Techniques in Space Plasmas: Particles*: Vol 2[M]. [S.l.]: American Geophysical Union, 1998.
- 30 Němeček Z, Šafránková J, Zastenker G. Dynamics of the earth's bow shock position[J/OL]. *Advances in Space Research*, 1988, 8(9-10): 167-170. [http://dx.doi.org/10.1016/0273-1177\(88\)90127-5](http://dx.doi.org/10.1016/0273-1177(88)90127-5).
- 31 Šafránková J, Jelínek K, Němeček Z. The bow shock velocity from two-point measurements in frame of the interball project[J/OL]. *Advances in Space Research*, 2003, 31(5): 1377-1382. [http://dx.doi.org/10.1016/S0273-1177\(02\)00951-1](http://dx.doi.org/10.1016/S0273-1177(02)00951-1).
- 32 Berchem J, Russell C T. The thickness of the magnetopause current layer: ISEE 1 and 2 observations[J/OL]. *Journal of Geophysical Research*, 1982, 87(A4): 2108. <http://dx.doi.org/10.1029/JA087iA04p02108>.
- 33 Sergeev V A, Angelopoulos V, Gosling J T, et al. Detection of localized, plasma-depleted flux tubes or bubbles in the midtail plasma sheet[J/OL]. *Journal of Geophysical Research: Space Physics*, 1996, 101(A5): 10817-10826. <https://onlinelibrary.wiley.com/doi/abs/10.1029/96JA00460>.
- 34 Forbes T G, Hones Jr. E W, Bame S J, et al. Substorm-related plasma sheet motions as determined from differential timing of plasma changes at the Isee satellites[J/OL]. *Journal of Geophysical Research: Space Physics*, 1981, 86(A5): 3459-3469. <https://onlinelibrary.wiley.com/doi/abs/10.1029/JA086iA05p03459>.
- 35 Sergeev V A, Mitchell D G, Russell C T, et al. Structure of the tail plasma/current sheet at ~ 11 RE and its changes in the course of a substorm[J/OL]. *Journal of Geophysical Research: Space Physics*, 1993, 98(A10): 17345-17365. <https://onlinelibrary.wiley.com/doi/abs/10.1029/93JA01151>.

-
- 36 Sibeck D G, Prech L, Safrankova J, et al. Two-point measurements of the magnetopause: Interball observations[J/OL]. *Journal of Geophysical Research*, 2000, 105(A1): 237-244. <http://dx.doi.org/10.1029/1999JA900390>.
- 37 Escoubet C P, Fehringer M, Goldstein M. Introduction: The Cluster mission[J/OL]. *Ann. Geophys.*, 2001, 19(10/12): 1197-1200. <http://dx.doi.org/10.5194/angeo-19-1197-2001>.
- 38 Malcolm W. Dunlop, Timothy I. Woodward. Analysis Methods for Multi-Spacecraft Data[M] // G. Paschmann, Patrick W. Daly. . Noordwijk, The Netherlands : ESA Publications Division, 1998 : 185.
- 39 Sonnerup B U, Haaland S E, Paschmann G. Multi-Spacecraft Analysis Methods Revisited[M] // G[']otz Paschmann, Patrick W. Daly. . [S.l.] : ESA Publications Division, 2008 : 1-15.
- 40 Kruparova O, Krupar V, Šafránková J, et al. Statistical Survey of the Terrestrial Bow Shock Observed by the Cluster Spacecraft[J/OL]. *JGR*, 2019, 124(3): 1539-1547. <http://dx.doi.org/10.1029/2018JA026272>.
- 41 Haaland S E, Sonnerup B U O, Dunlop M W, et al. Four-spacecraft determination of magnetopause orientation, motion and thickness: comparison with results from single-spacecraft methods[J/OL]. *Annales Geophysicae*, 2004, 22(4): 1347-1365. <https://angeo.copernicus.org/articles/22/1347/2004/>.
- 42 Nakamura R, Baumjohann W, Klecker B, et al. Motion of the dipolarization front during a flow burst event observed by Cluster[J/OL]. *Geophysical Research Letters*, 2002, 29(20): 3-4. <https://onlinelibrary.wiley.com/doi/abs/10.1029/2002GL015763>.
- 43 Sergeev V, Runov A, Baumjohann W, et al. Current sheet flapping motion and structure observed by Cluster[J/OL]. *Geophysical Research Letters*, 2003, 30(6). <https://onlinelibrary.wiley.com/doi/abs/10.1029/2002GL016500>.
- 44 Harvey C C. Analysis Methods for Multi-Spacecraft Data[M] // G. Paschmann, Patrick W. Daly. . Noordwijk, The Netherlands : ESA Publications Division, 1998 : 307.

- 45 Dunlop M W, Balogh A, Glassmeier K-H, et al. Four-point Cluster application of magnetic field analysis tools: The Curlometer[J/OL]. *Journal of Geophysical Research: Space Physics*, 2002, 107(A11): SMP 23-14. <https://onlinelibrary.wiley.com/doi/abs/10.1029/2001JA005088>.
- 46 Shen C, Li X, Dunlop M, et al. Analyses on the geometrical structure of magnetic field in the current sheet based on cluster measurements[J/OL]. *JGR*, 2003, 108(A5). <http://dx.doi.org/https://doi.org/10.1029/2002JA009612>.
- 47 Shen C, Dunlop M, Li X, et al. New approach for determining the normal of the bow shock based on Cluster four-point magnetic field measurements[J/OL]. *JGR*, 2007, 112(A3). <http://dx.doi.org/https://doi.org/10.1029/2006JA011699>.
- 48 Shen C, Li X, Dunlop M, et al. Magnetic field rotation analysis and the applications[J/OL]. *JGR*, 2007, 112(A6). <http://dx.doi.org/10.1029/2005JA011584>.
- 49 Dunlop M W, Eastwood J P. Multi-Spacecraft Analysis Methods Revisited[M] // G'otz Paschmann, Patrick W. Daly. . [S.l.]: ESA Publications Division, 2008 : 17-25.
- 50 Shen C, Dunlop M W. Multi-Spacecraft Analysis Methods Revisited[M] // G'otz Paschmann, Patrick W. Daly. . [S.l.]: ESA Publications Division, 2008 : 27-32.
- 51 Shen C, Zeng G, Zhang C, et al. Determination of the Configurations of Boundaries in Space[J/OL]. *Journal of Geophysical Research: Space Physics*, 2020, 125(9). <http://dx.doi.org/10.1029/2020JA028163>.
- 52 Dunlop M W, Wang T, Dong X, et al. Magnetospheres in the Solar System[M/OL] // Nicolas André Romain Maggiolo H H D T W Y Z L J P. . [S.l.]: Wiley, 2021 : 637-656. <http://dx.doi.org/10.1002/9781119815624.ch40>.
- 53 Yang Y Y, Shen C, Dunlop M, et al. Storm time current distribution in the inner equatorial magnetosphere: THEMIS observations[J/OL]. *JGR*, 2016, 121(6): 5250-5259. <http://dx.doi.org/10.1002/2015ja022145>.

-
- 54 Dunlop M W, Yang J-Y, Yang Y-Y, et al. Simultaneous field-aligned currents at Swarm and Cluster satellites[J/OL]. *Geophysical Research Letters*, 2015, 42(10): 3683-3691. <https://onlinelibrary.wiley.com/doi/abs/10.1002/2015GL063738>.
- 55 Dunlop M W, Balogh A. Magnetopause current as seen by Cluster[J/OL]. *Annales Geophysicae*, 2005, 23(3): 901-907. <https://angeo.copernicus.org/articles/23/901/2005/>.
- 56 Runov A, Sergeev V A, Nakamura R, et al. Local structure of the magnetotail current sheet: 2001 Cluster observations[J/OL]. *Ann. Geophys.*, 2006, 24(1): 247-262. <https://www.ann-geophys.net/24/247/2006/>.
- 57 Nakamura R, Varsani A, Genestreti K J, et al. Multiscale Currents Observed by MMS in the Flow Braking Region[J/OL]. *Journal of Geophysical Research: Space Physics*, 2018, 123(2): 1260-1278. <https://onlinelibrary.wiley.com/doi/abs/10.1002/2017JA024686>.
- 58 Turner D L, Cohen I J, Bingham S T, et al. Characteristics of Energetic Electrons Near Active Magnetotail Reconnection Sites: Tracers of a Complex Magnetic Topology and Evidence of Localized Acceleration[J/OL]. *Geophysical Research Letters*, 2021, 48(2): e2020GL090089. <https://onlinelibrary.wiley.com/doi/abs/10.1029/2020GL090089>.
- 59 Wang G Q, Zhang T L, Wu M Y, et al. Field-Aligned Currents Originating From the Chaotic Motion of Electrons in the Tilted Current Sheet: MMS Observations[J/OL]. *Geophysical Research Letters*, 2021, 48(9): e2020GL088841. <https://onlinelibrary.wiley.com/doi/abs/10.1029/2020GL088841>.
- 60 Qi Y, Russell C T, Jia Y-D, et al. Temporal Evolution of Flux Tube Entanglement at the Magnetopause as Observed by the MMS Satellites[J/OL]. *Geophysical Research Letters*, 2020, 47(23). <http://dx.doi.org/10.1029/2020GL090314>.
- 61 Kieokaew R, Foullon C. Kelvin-Helmholtz Waves Magnetic Curvature and Vorticity: Four-Spacecraft Cluster Observations[J/OL]. *Journal of Geophysical Research*

- search: Space Physics, 2019, 124(5): 3347-3359. <http://dx.doi.org/10.1029/2019JA026484>.
- 62 Kieokaew R, Lavraud B, Foullon C, et al. Magnetic Reconnection Inside a Flux Transfer Event-Like Structure in Magnetopause Kelvin-Helmholtz Waves[J/OL]. Journal of Geophysical Research: Space Physics, 2020, 125(6): e2019JA027527. <https://onlinelibrary.wiley.com/doi/abs/10.1029/2019JA027527>.
- 63 Wang G Q, Zhang T L, Wu M Y, et al. Study of the Electron Velocity Inside Sub-Ion-Scale Magnetic Holes in the Solar Wind by MMS Observations[J/OL]. Journal of Geophysical Research: Space Physics, 2020, 125(10). <http://dx.doi.org/10.1029/2020JA028386>.
- 64 Angelopoulos V. The THEMIS Mission[J/OL]. Space Sci. Rev., 2008, 141(1-4): 5-34. <http://dx.doi.org/10.1007/s11214-008-9336-1>.
- 65 Burch J L, Moore T E, Torbert R B, et al. Magnetospheric Multiscale Overview and Science Objectives[J/OL]. Space Sci. Rev., 2015, 199(1-4): 5-21. <http://dx.doi.org/10.1007/s11214-015-0164-9>.
- 66 Kieokaew R, Foullon C, Lavraud B. Four-Spacecraft Magnetic Curvature and Vorticity Analyses on Kelvin-Helmholtz Waves in MHD Simulations[J/OL]. Journal of Geophysical Research: Space Physics, 2018, 123(1): 513-529. <http://dx.doi.org/10.1002/2017JA024424>.
- 67 He J-S, Tu C-Y, Tian H, et al. A magnetic null geometry reconstructed from Cluster spacecraft observations[J/OL]. Journal of Geophysical Research: Space Physics, 2008, 113(A5): n/a-n/a. <http://dx.doi.org/10.1029/2007JA012609>.
- 68 Fu H S, Vaivads A, Khotyaintsev Y V, et al. How to find magnetic nulls and reconstruct field topology with MMS data?[J/OL]. Journal of Geophysical Research: Space Physics, 2015, 120(5): 3758-3782. <https://onlinelibrary.wiley.com/doi/abs/10.1002/2015JA021082>.
- 69 Kaufmann R L, Ball B M, Paterson W R, et al. Plasma sheet thickness and electric currents[J/OL]. JGR, 2001, 106(A4): 6179-6193. <http://dx.doi.org/10.1029/2000ja000284>.

-
- 70 Ganushkina N Y, Liemohn M W, Dubyagin S, et al. Defining and resolving current systems in geospace[J/OL]. *Ann. Geophys.*, 2015, 33(11): 1369-1402. <http://dx.doi.org/10.5194/angeo-33-1369-2015>.
- 71 Argall M, Shuster J, Dors I, et al. How neutral is quasi-neutral: Charge Density in the Reconnection Diffusion Region Observed by MMS[J/OL]. *Earth and Space Science Open Archive*, 2019: 1. <https://doi.org/10.1002/essoar.10501410.1>.
- 72 Shen C, Zhou Y, Gao L, et al. Measurements of the Net Charge Density of Space Plasmas[J/OL]. *Journal of Geophysical Research: Space Physics*, 2021, 126(12). <http://dx.doi.org/10.1029/2021JA029511>.
- 73 Parks G. *Physics Of Space Plasmas-An Introduction*[M]. Second. [S.l.]: Westview Press, 2004.
- 74 Srivastava A K, Mishra S K, Jelínek P. The Prominence Driven Forced Reconnection in the Solar Corona and Associated Plasma Dynamics[J/OL]. *The Astrophysical Journal*, 2021, 920(1): 18. <http://dx.doi.org/10.3847/1538-4357/ac1519>.
- 75 Yu S, Chen B, Reeves K K, et al. Magnetic Reconnection during the Post-impulsive Phase of a Long-duration Solar Flare: Bidirectional Outflows as a Cause of Microwave and X-Ray Bursts[J/OL]. *The Astrophysical Journal*, 2020, 900(1): 17. <http://dx.doi.org/10.3847/1538-4357/aba8a6>.
- 76 Zou P, Jiang C, Wei F, et al. Continuous Null-point Magnetic Reconnection Builds Up a Torus Unstable Magnetic Flux Rope Triggering the X9.3 Flare in Solar AR 12673[J/OL]. *The Astrophysical Journal*, 2020, 890(1): 10. <http://dx.doi.org/10.3847/1538-4357/ab6aa8>.
- 77 Priest E R, Chitta L P, Syntelis P. A Cancellation Nanoflare Model for Solar Chromospheric and Coronal Heating[J/OL]. *The Astrophysical Journal Letters*, 2018, 862(2): L24. <http://dx.doi.org/10.3847/2041-8213/aad4fc>.
- 78 Shen C, Zhang C, Rong Z, et al. Nonlinear Magnetic Gradients and Complete Magnetic Geometry From Multispacecraft Measurements[J/OL]. *Journal of Geophysical Research: Space Physics*, 2021, 126(8). <http://dx.doi.org/10.1029/2020JA028846>.

-
- 79 Liu Y Y, Fu H S, Olshevsky V, et al. SOTE: A Nonlinear Method for Magnetic Topology Reconstruction in Space Plasmas[J/OL]. The Astrophysical Journal Supplement Series, 2019, 244(2): 31. <http://dx.doi.org/10.3847/1538-4365/ab391a>.
- 80 Torbert R B, Dors I, Argall M R, et al. A New Method of 3-D Magnetic Field Reconstruction[J/OL]. Geophys. Res. Lett., 2020, 47(3). <http://dx.doi.org/10.1029/2019GL085542>.
- 81 Ganushkina N Y, Liemohn M W, Dubyagin S. Current Systems in the Earth's Magnetosphere[J/OL]. Rev. Geophys., 2018, 56(2): 309-332. <http://dx.doi.org/10.1002/2017RG000590>.
- 82 Shen C, Zhou Y, Ma Y, et al. A General Algorithm for the Linear and Quadratic Gradients of Physical Quantities Based on 10 or More Point Measurements[J/OL]. Journal of Geophysical Research: Space Physics, 2021, 126(6). <http://dx.doi.org/10.1029/2021JA029121>.
- 83 Chanteur G. Analysis Methods for Multi-Spacecraft Data[M] // G. Paschmann, Patrick W. Daly. . Noordwijk, The Netherlands : ESA Publications Division, 1998 : 349.
- 84 Jean-Louis Pinçon, Uwe Motschmann. Analysis Methods for Multi-Spacecraft Data[M] // G. Paschmann, Patrick W. Daly. . Noordwijk, The Netherlands : ESA Publications Division, 1998 : 65.
- 85 Lundquist S. Magnetohydrostatic fields[J]. Ark. Fys., 1950, 2: 361-365.

INNOVATIVE ACHIEVEMENTS FOR MASTER

1. Shen C, Zhou Y, Ma Y, et al. A General Algorithm for the Linear and Quadratic Gradients of Physical Quantities Based on 10 or More Point Measurements[J/OL]. Journal of Geophysical Research: Space Physics, 2021, 126(6).

哈尔滨工业大学学位论文原创性声明和使用权限

学位论文原创性声明

本人郑重声明：此处所提交的学位论文《基于空间多点探测的物理场的一次和二次梯度算法的分析研究》，是本人在导师指导下，在哈尔滨工业大学攻读学位期间独立进行研究工作所取得的成果，且学位论文中除已标注引用文献的部分外不包含他人完成或已发表的研究成果。对本学位论文的研究工作做出重要贡献的个人和集体，均已在文中以明确方式注明。

作者签名：周宇飞

日期：2021年12月28日

学位论文使用权限

学位论文是研究生在哈尔滨工业大学攻读学位期间完成的成果，知识产权归属哈尔滨工业大学。学位论文的使用权限如下：

(1) 学校可以采用影印、缩印或其他复制手段保存研究生上交的学位论文，并向国家图书馆报送学位论文；(2) 学校可以将学位论文部分或全部内容编入有关数据库进行检索和提供相应阅览服务；(3) 研究生毕业后发表与此学位论文研究成果相关的学术论文和其他成果时，应征得导师同意，且第一署名单位为哈尔滨工业大学。

保密论文在保密期内遵守有关保密规定，解密后适用于此使用权限规定。

本人知悉学位论文的使用权限，并将遵守有关规定。

作者签名：周宇飞

日期：2021年12月28日

导师签名：沈逸

日期：2021年12月31日